Document downloaded from:

http://hdl.handle.net/10251/202049

This paper must be cited as:

Gamero, P.; Cantero-Chinchilla, FN.; Bergillos, RJ.; Castro-Orgaz, O.; Dey, S. (2022). Shallow-water lee-side waves at obstacles: Experimental characterization and turbulent non-hydrostatic modeling using weighted-averaged residual equations. Environmental Modelling & Software. 155:1-16. https://doi.org/10.1016/j.envsoft.2022.105422

The final publication is available at

https://doi.org/10.1016/j.envsoft.2022.105422

Copyright Elsevier

Additional Information

# Shallow-water lee-side waves at obstacles: Experimental characterization and turbulent non-hydrostatic modeling using weighted-averaged residual equations

Pedro Gamero[a], Francisco N. Cantero-Chinchilla[a*], Rafael J. Bergillos[b], Oscar Castro-Orgaz[a], and Subhasish Dey[c]

[a] *Hydraulic Engineering Area, Department of Agronomy, University of Córdoba, Rabanales Campus, Leonardo da Vinci Building, 14071 Córdoba, Spain*

[b] *Research Institute of Water and Environmental Engineering (IIAMA), Universitat Politècnica de València, 46022, Valencia, Spain*

[c] *Department of Civil Engineering, Indian Institute of Technology Kharagpur, West Bengal, 721302, India*

---

*Corresponding author.
E-mail address: z12cachf@uco.es (F. N. Cantero-Chinchilla)

Preprint submitted to Environmental Modelling & Software

## Abstract

The flow over uneven topography is a problem of interest in environmental fluid flow modeling, including flows over river bedforms, exchange flows over oceanic sills or the airflow over mountains. The common experimental procedure to investigate these flows, moving a small obstacle in a laboratory flume, yields experimental difficulties, whereas modeling using non-linear shallow flow equations does not explain all the flow phenomena. Novel alternative procedures are presented for the experimentation and shallow water representation of flow interaction with obstacles. A large-scale obstacle model is constructed in a dam-break set-up, and used to generate flow phenomena over topography, including dispersive and broken surges, wave reflection, hydraulic jumps and non-hydrostatic sill overflows. Simulations are conducted with a shallow-water weighted-averaged residual flow software for turbulent flows. The proposed software reproduces the experiments satisfactorily, supporting its use in modeling, whereas the new experimental database can be used by modelers to test their software.

*Keywords:* non-hydrostatic flows; laboratory experiments; weighted-averaged residual equations; lee-side waves; obstacles

---

## Highlights

- A novel experimental procedure to study wave interaction with obstacles is presented
- A new experimental database of utility for software validation by environmental fluid flow modelers is generated
- A new weighted-averaged residual flow software for turbulent flow over obstacles is presented

## Software availability

- Name of software: Waves Transformation Model Software

- Contact emails: ag2gaojp@uco.es, z12cachf@uco.es, ag2caoro@uco.es

- Requirements: MATLAB

- Availability: The software platform is freely available at https://github.com/Frncch/Waves_Transformation_Model_Software

## 1. Introduction

The study of two-dimensional shallow-water flows over obstacles is relevant in several branches of environmental mechanics, as in the river flow over bedforms, like dunes and antidunes, in oceanographic exchange flows over a seamount, or in the mesoscale atmospheric flow past a steep mountain (Nadiga et al., 1996; Zhu and Lawrence, 1998). A common mathematical procedure to study these flows consists in set instantaneously an obstacle into an initially steady and uniform stream, and then study the time-dependent flow adjustment that takes place and the ensuing asymptotic steady-state (Long, 1954; 1970; Pratt, 1984; Nadiga et al., 1996), typically using either the shallow-water dispersionless Saint-Venant equations (Houghton and Kasahara 1968, Pratt 1984; Cea et al., 2011) or the dispersive Serre–Green–Naghdi (SGN) equations (Nadiga et al. 1996). The experimental procedure to generate these flows consists in rapidly accelerate up to a target constant velocity an obstacle initially at rest in a flume filled with water (Long, 1954; 1970). In Long's (1970) experiments, the obstacle was moved in the flume by a thin line wrapped around a cylindrical winder driven by a motor. The velocity of obstacle displacement was experimentally determined by counting the revolutions, and then this velocity was used to deduce the flow patterns observed moving with the obstacle, e.g., the equivalent flow with a static obstacle (Long, 1970). This experimental procedure is however not simple, and is prone to large number of problems. First, the experimental design is only economical thus feasible using small obstacles, e.g., in Long's (1970) experiments rather small ones, only of 9.1 and 2 cm high, were installed. Second, the wave-generation around the obstacle is induced by moving it, thereby producing leakage at the joins with the flume sidewalls and at the obstacle bottom. These problems are hardly solvable, especially for high Froude numbers involving supercritical flows (Long, 1970). In addition to the experimental configuration problems, the quality and type of experimental data that can be extracted from this set-up are limited. For example, instantaneous free surface profile measurements of these flows are not available in the literature, which would be especially desirable to compare with the theoretical predictions of shallow-water models. The typical data extracted from Long's experiments consists only in the upstream and crest flow depths, as well as the Froude number (Long 1970). Further, the flow over a curved obstacle involves vertical accelerations and thus non-hydrostatic bed pressures (Nadiga et al., 1996; Zhu and Lawrence, 1998; Gamero et al., 2020), which should be experimentally determined. However, in Long's (1970) set-up, the obstacle was moving, thus it would have been a very challenging task to take bed-pressure measurements for the asymptotic steady flow over the obstacle by installing pressure taps at the obstacle surface. Note that the instantaneous appearance of an obstacle in a stream is not a realistic mechanism of forcing in geophysical fluid flows, despite its wide use by environmental flow modelers (Pratt, 1984). Thus, an alternative method to study wave interaction with obstacles in environmental flows was considered, as commented below.

During the time-dependent flow adjustment towards a steady flow over an obstacle, shocks are formed moving upstream and downstream of it (Long, 1954; 1970;

Houghton and Kasahara, 1968; Pratt, 1984; Nadiga et al., 1996), with a transition from subcritical to supercritical flow conditions occurring in the vicinity of the obstacle crest (Naghdi and Vongsarnpigoon, 1986; Zhu and Lawrence, 1998). At the lee-side of the obstacle the flow typically changes from supercritical to subcritical flow conditions trough a moving shock displacing away from the obstacle. The shocks at the lee-side of the obstacle may be either undular or broken, depending on the Froude number. These instantaneous waves are hardly characterized experimentally in the literature, and simulations using SGN models (Nadiga et al., 1996) showed inability of this shallow-water representation to mimic the turbulent flow processes occurring, given that wave breaking (Bayon et al., 2016; Gualtieri and Chanson, 2021) is not modeled. If the Froude number at the lee-side face of the obstacle is high, turbulent breaking occurs, and the undular waves predicted by SGN models become unrealistic (Nadiga et al., 1996; Castro-Orgaz and Chanson, 2017). Turbulent breaking at the lee-side of obstacles is important, as for example in a oceanographic flow of salt water moving over a sill in a fresh water environment (Farmer and Denton, 1985; Denton, 1987). In these flows, turbulent breaking of the lee-side waves induces mixing between layers and, thus, provides nutrients and dissolved oxygen for the deep water; it further affects the dispersion of any pollutant. Therefore, a shallow-water turbulent flow model with ability to simulate both undular and broken waves is needed to simulate flow over obstacles. The main aim of this research is to characterize the complex features of open-channel flows downstream of a bottom hump, which cannot be simulated by the standard shallow water equations.

Given that the lee-side obstacle waves are neither characterized with detailed experiments nor simulated with shallow-water turbulent non-hydrostatic models, the experimental and numerical modeling of these flows are the two major objectives of this work.

As described in section (ii) of this work, lee-side obstacle waves are generated experimentally in a large-scale obstacle model with a new and entirely different procedure from that of Long's: A dam-break-like set-up was installed in a long experimental flume, consisting in a gate installed downstream of the obstacle and equipped with an instantaneous opening mechanism, thereby permitting to generate lee-side waves once the gate was opened instantaneously. The type of waves generated at the lee face of the obstacle depends on the upstream water depth at the gate, which was an experimental parameter to generate the flows. This new experimental procedure is different from that of Long, but it permits to generate waves at the lee-side of obstacles and study their interaction with it, which was the major objective in Long's set-up. This new experimental set-up has the major advantage of permitting to execute accurate experiments at a large-scale obstacle model and collecting high-quality data, including the instantaneous free surface profiles and the steady bed-pressures over the obstacle. Note that the instantaneous appearance of an obstacle in a stream as in Long's approach is not a realistic flow; however, this experimental procedure, in addition to serve to study the flow adjustment over an obstacle in response to the generated waves, conceptually represents an abrupt drop in the water levels around the obstacle in response to a downstream forcing. The value of the new experimental dataset generated in this work relies on two major aspects: (1) In Long's (1970) experiments, the free surface profiles are presented only qualitatively using photos, but measurements are not available, given the complications to take such readings with a moving obstacle; and (2) there is no previous work in the literature to the authors' knowledge, where waves over a curved obstacle are generated with a dam-break like setting.

Shallow-water modeling is considered in section (iii); A shallow-water non-hydrostatic flow model was constructed from the Reynolds-Averaged Navier-Stokes equations by using a weighted-averaged residual method of Galerkin type. The model accounts for a non-hydrostatic fluid pressure, which has the ability to model undular waves. Further, the turbulent velocity profile and turbulent stresses are modeled in the weighted-averaged equations, permitting to simulate broken waves during the flow adjustment over the obstacle. A high-resolution finite volume-finite difference numerical solver is developed and extensively verified in section (iv) using both benchmark numerical tests and the new experimental measurements conducted in this work. Conclusions are presented in section (v). The model software is freely available on GitHub (https://github.com/Frncch/Waves_Transformation_Model_Software), whereas the experimental database is provided as supplementary material in the file "Experiments_EMS2022.xls".

## 2. Experimental characterization

### *2.1 Experimental flume and equips*

The experiments were conducted in a 15-m-long, 1-m-high, 1-m-width tilting experimental flume in the Hydraulics laboratory at the University of Córdoba, Spain. A reduction of the flume width to 0.405 m was accomplished by a moving division wall (Fig. 1), and the flume slope for the experimental series conducted was 0.0015 m/m. The tailwater portion of the flume from 9.634 m to 15 m downstream the inlet section was structurally a cantilever, and the beam deformation, though small, was considered in the simulations to accurately define the actual bed profile of the flume.

The flume was equipped with a recirculation pump of 0.078 $m^3/s$ maximum discharge connected to a downstream water tank, allowing to work in closed-circuit. A water tank with flow straightener was located at the flume inlet to reduce flow disturbances. The tailgate of the flume was fully open or closed, depending on the type of experiment, e.g., with or without reflection at the flume end. A large-scale obstacle of Gaussian profile $z_{bG} = 0.209 \cdot \exp[-1/2 \cdot ((x - x_{crest})/0.254)^2]$, where $z_{bG}$ is the local obstacle height above the flume bed and $x_{crest}$ the longitudinal location of the crest, was installed at $x_{crest} = 6.565$ m. A Gaussian obstacle shape was selected because it permits to mathematically adjust their parameters in the design phase prior to construction. In this way, it was possible to adjust the crest curvature until producing the desired degree of non-hydrostaticity in the flow over the obstacle. Further, this shape is easy to construct in metal by a manufacturer. Along the longitudinal symmetry axis of the obstacle 17 piezometric tapings were installed to take bottom pressure head reading in a piezometric panel.

The flume was equipped with a dam-break like set-up consisting in a sluice gate of high-speed release induced by a pneumatic drive system. The gate opening time was less than 0.15 s in all the experiments conducted in this work, thus the opening operation can be considered instantaneous. A high-speed camera Fastec Ts5 with 50 mm focal length lens to avoid image distortion capturing at up to 253 fps at maximum resolution was used to characterize the movement of the gate and ensure that the operation can be considered fast enough to reproduce dam-break like waves.

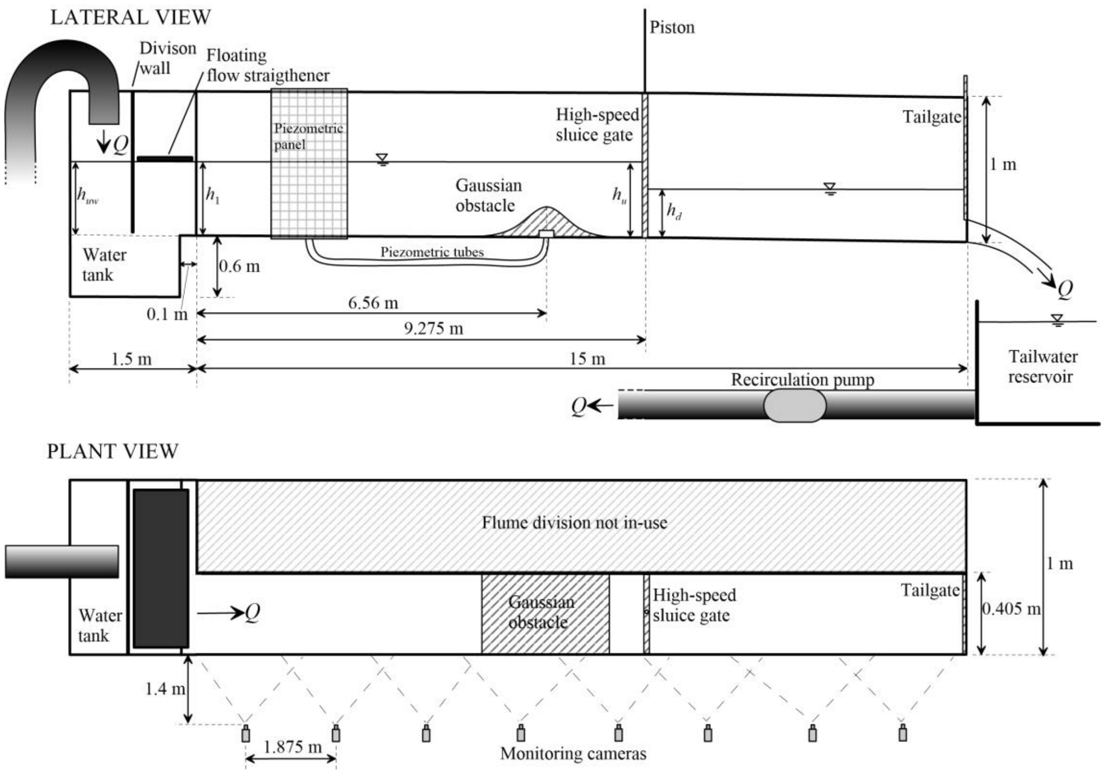


**Fig. 1**. Sketch of experimental set-up, showing static water levels at initiation of unsteady flow experiments

Flow visualization during the experiments was accomplished through the eight lateral crystal windows, 1.875-m-wide by 0.975-m-high, of the flume. Each window was monitored by a camera perpendicularly installed in front of the flume (Fig. 1). The monitoring video system comprises eight Basler Ace acA1920-40uc cameras, with 6 mm focal length lens to allow capturing the whole width of each lateral crystal window, recording 40 frames-per-second (fps) maximum at full resolution, and a laptop Intel® Core™ i7-9750H with software for image capture, synchronization, assembling and processing. The system automatically assembles the images collected by the 8 cameras in a synchronized way, correcting distortion errors and thereby providing instantaneous experimental images of the 15 meters of flume.

The novelty of this experimental research is in the experimental procedure and set-up used to generate waves evolving over obstacles. In Long's (1970) classical experiments, an obstacle is moved in a flume filled with initially still water (Pratt and Whitehead 2007), whereas in this work we have generated the unsteady waves over a fixed obstacle using a dam-break like set-up.

### *2.2 Experimental series*

Two kinds of experimental series were produced. The first series consisted of dam-break wave experiments generated by using the high-speed sluice gate with no inlet flow ($Q$ = 0), and the tailgate fully closed to allow wave reflection. The second series consisted of steady flow experiments with various $Q$ up to the maximum discharge, with the high-speed gate deactivated (no operation, positioned above the flume) and the tailgate fully opened.

**Table 1**. Test series characteristics for dam-break experiments

| Test | $h_u$ (m) | $h_d$ (m) | $r$ (-) |
|---|---|---|---|
| 1 | 0.302 | 0.12 | 0.397 |
| 2 | 0.3 | 0.18 | 0.6 |
| 3 | 0.3 | 0.24 | 0.8 |
| 4 | 0.3 | 0 | 0 |

The dam break experiments were designed using different downstream to upstream water depth ratios, $r = h_d/h_u$, with zero inlet discharge and closed tailgate, which were organized in tests series comprising $r$ = 0, 0.397, 0.6, and 0.8 (Table 1). First, the flume was filled with water up to the level $h_d$ considered, and then the high-speed sluice gate closed. Thereafter, the upstream side of the gate further filled up to the desired $r$ was fixed. Afterwards, the high-speed sluice gate was released (Fig. 2a).

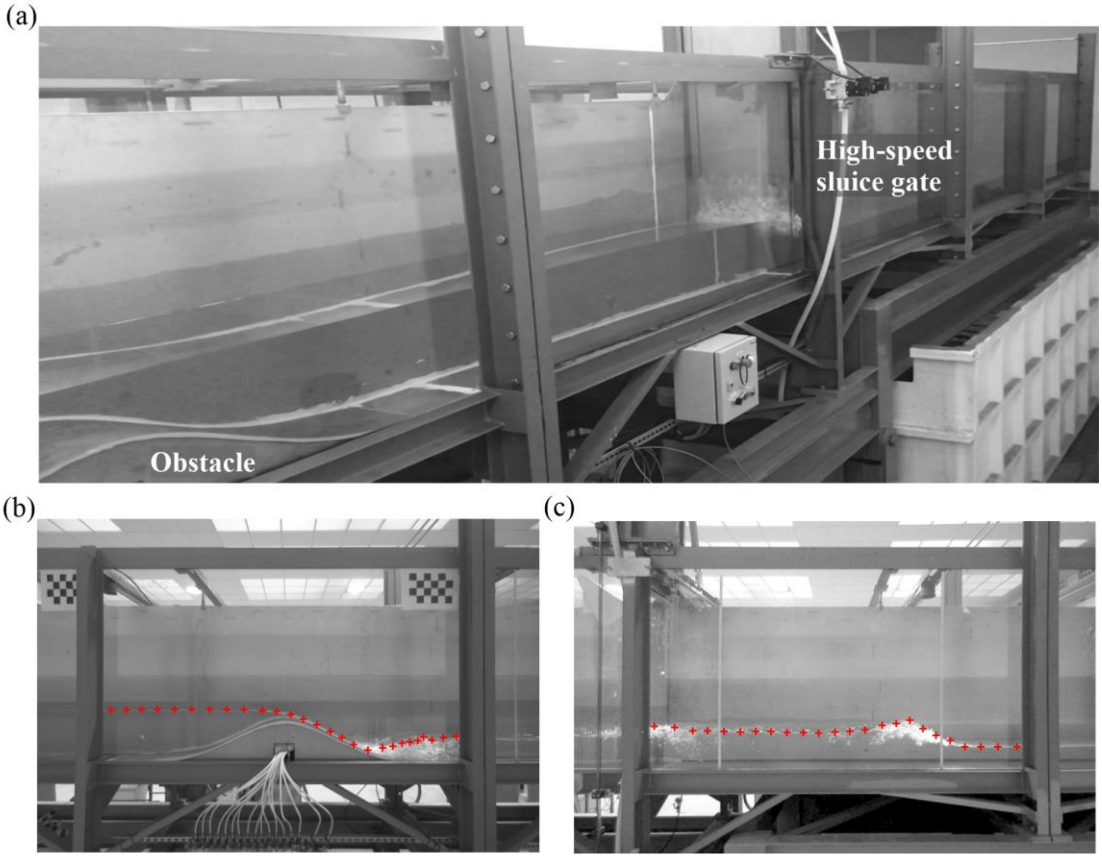


**Fig. 2**. Experimental tests: (a) photograph of the test 1 right after the sluice gate release, (b) corrected image of camera 4 at $t$ = 6 s with unsteady hydraulic jump at the toe of the obstacle, and (c) corrected image of camera 6 at $t$ = 1 s in test 1 with the advancing dam break bore. Digitized data points marked by red crosses.

The monitoring system was set to record images at 25 fps, which was enough to take a detailed experimental characterization of the unsteady water waves. Each test was recorded during 12 seconds, enabling to capture all the relevant hydraulic processes, namely the positive and negative dam-break wave generation, wave reflection at the closed tailwater gate, formation of a hydraulic jump at the lee-side of the obstacle, and interaction of the reflected wave with the flow developing over the obstacle.

Once the images collected by the system of cameras were assembled and distortion errors were corrected for selected instants of time, they were used to extract the instantaneous flow profiles (Fig. 2b, c). The free surface was digitalized from the images over the free surface curve in the crystal wall using Golden Software Grapher® 13.3.754. By trial-and-error calibration tests, it was found that the procedure permits to measure the experimental flow profile with ± 0.1 cm accuracy. For illustration purposes, panoramic instants at $t$ = 1, 6 and 10 s for test 1 are shown in Fig. 3 using the corrected images of the cameras 4, 5 and 6 (from left to right in each subfigure).

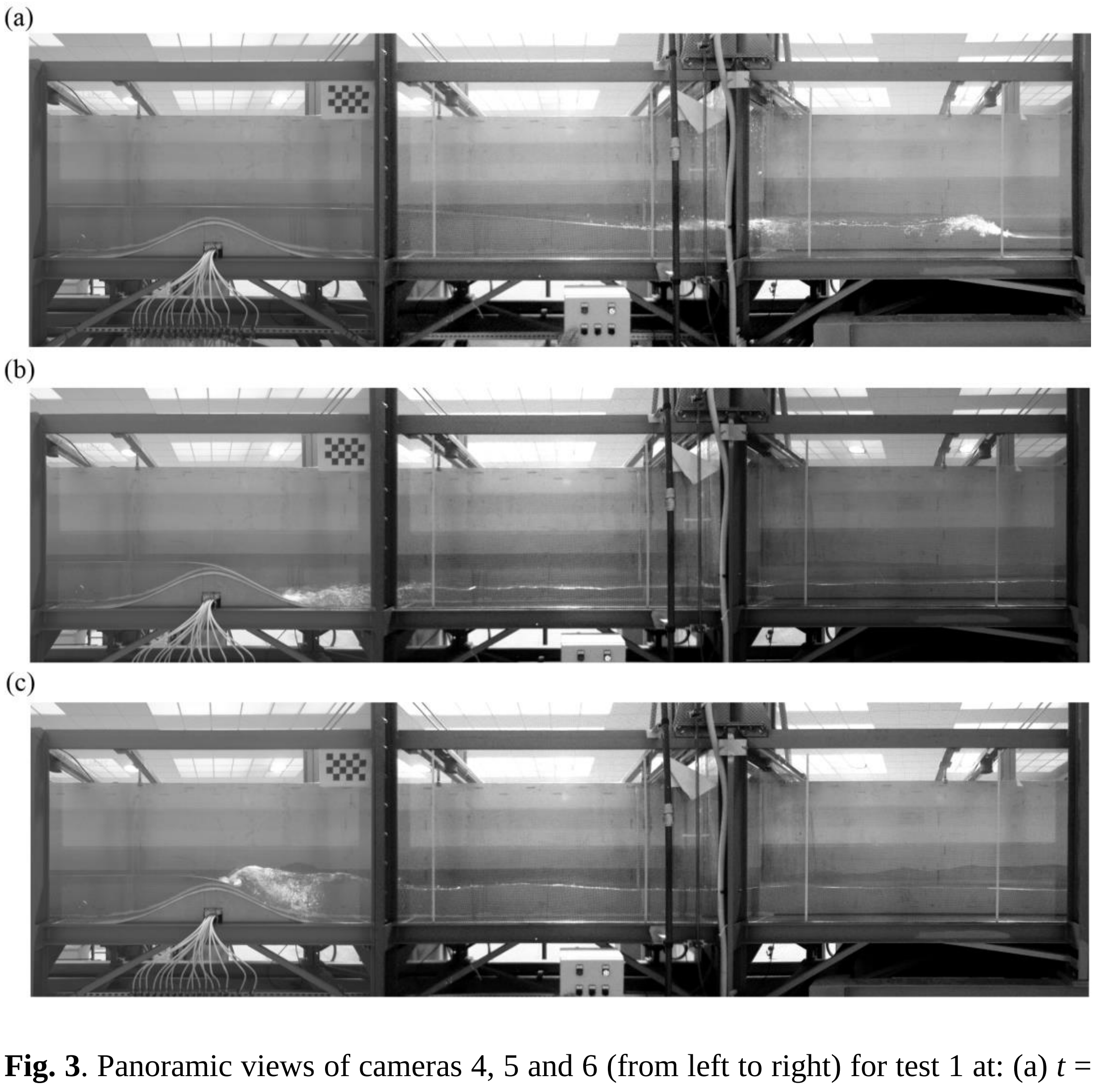


**Fig. 3**. Panoramic views of cameras 4, 5 and 6 (from left to right) for test 1 at: (a) $t$ = 1 s, (b) $t$ = 6 s, and (c) $t$ = 10 s. The piezometric tubes are shown in the left images.

An accurate modeling of the upstream boundary condition in the numerical solver requires use as input the time-variation of the static upstream water level at the inlet tank solid wall $h_{uw}$. This time-dependent variable was measured during the experiments with the high-speed camera Fastec Ts5, and from the ensuing measurements, the following 4th-order polynomial was found to describe inlet flow conditions: $h_{uw}$ (m) = $(0.0015 \cdot t^4 - 0.032 \cdot t^3 + 0.1656 \cdot t^2 - 0.2503 \cdot t + 0.0393 + 100 \cdot h_1)/100$ ($R^2 = 0.98$), where $h_{uw}$ is the flow depth at the upstream wall of the water tank, $t$ is the time and $h_1$ is the flow depth level at the upstream section of the flume (see Fig. 1).

Steady flow experiments were conducted with fully open tail- and high-speed sluice gates with various discharges up to the maximum of the system, 0.1826 $m^2$/s. The bed pressure head was measured by visual observation of a piezometric panel allowing readings of accuracy ± 0.1 cm.

## 3. Shallow-water turbulent flow modeling

### *3.1 Weighted-averaged residual equations*

Consider steady two-dimensional flow in a vertical plane (Fig. 4), as in the previously described experiments (Fig. 3). The modeling approximation pursued here entails the development of weighted-averaged residual equations from the RANS equations of turbulent free surface flow following Steffler and Jin (1993). In a first step, a sequence of Vertically Averaged and Moment (VAM) equations is produced by using the first shifted Legendre polynomial as test function, resulting (Steffler and Jin, 1993; Khan and Steffer, 1996a; b):

$$\frac{\partial h}{\partial t} + \frac{\partial h\bar{u}}{\partial x} = 0, \qquad (1)$$

$$\frac{\partial h\bar{u}}{\partial t} + \frac{\partial h\overline{u^2}}{\partial x} = -\frac{1}{\rho}\left[\frac{\partial h\left(\bar{p} - \bar{\sigma}_x\right)}{\partial x} + \left(p_b - \sigma_{xb}\right)\frac{\partial z_b}{\partial x} + \tau_{xzb}\right], \qquad (2)$$

$$\frac{\partial h\bar{w}}{\partial t}+\frac{\partial h\overline{uw}}{\partial x}=\frac{1}{\rho}\left(p_b+\frac{\partial h\overline{\tau_{xz}}}{\partial x}+\tau_{xzb}\frac{\partial z_b}{\partial x}-\sigma_{zb}\right)-gh\,, \tag{3}$$

$$\frac{h}{2}\frac{\partial h}{\partial t}+\frac{\partial h\overline{zu}}{\partial x}-\bar{z}\frac{\partial h\bar{u}}{\partial x}-h\bar{w}=0\,, \tag{4}$$

$$\frac{\partial h\overline{zu}}{\partial t}+\frac{\partial h\overline{zu^2}}{\partial x}-\bar{z}\frac{\partial h\bar{u}}{\partial t}-\bar{z}\frac{\partial h\overline{u^2}}{\partial x}-h\overline{uw}=-\frac{1}{\rho}\left(\frac{\partial h\overline{zp}}{\partial x}-\bar{z}\frac{\partial h\bar{p}}{\partial x}-\frac{hp_b}{2}\frac{\partial z_b}{\partial x}\right)$$
$$+\frac{1}{\rho}\left(\frac{\partial h\overline{z\sigma_x}}{\partial x}-\bar{z}\frac{\partial h\overline{\sigma_x}}{\partial x}-\frac{h\sigma_{xb}}{2}\frac{\partial z_b}{\partial x}+\frac{h\tau_{xzb}}{2}-h\overline{\tau_{xz}}\right), \tag{5}$$

$$\frac{\partial h\overline{zw}}{\partial t}+\frac{\partial h\overline{zuw}}{\partial x}-\bar{z}\frac{\partial h\bar{w}}{\partial t}-\bar{z}\frac{\partial h\overline{uw}}{\partial x}-h\overline{w^2}=-\frac{h}{\rho}\left(\frac{p_b}{2}-\bar{p}\right)$$
$$+\frac{1}{\rho}\left(\frac{\partial h\overline{z\tau_{xz}}}{\partial x}-\bar{z}\frac{\partial h\overline{\tau_{xz}}}{\partial x}-\frac{h\tau_{xzb}}{2}\frac{\partial z_b}{\partial x}+\frac{h\sigma_{zb}}{2}-h\overline{\sigma_z}\right), \tag{6}$$

where $x$ and $z$ are the horizontal and vertical Cartesian coordinates, respectively; $u(x, z, t)$ and $w(x, z, t)$ are the horizontal and vertical velocity components; $z_b(x)$ is the bed profile; $h(x, t)$ is the flow depth; $p(x, z, t)$ is the fluid pressure; $p_b(x, t)$ is bottom pressure; $\tau(x, z, t)$ and $\sigma(x, z, t)$ are the Reynolds tangential and normal stresses, respectively; $\rho$ is the fluid density; $g$ is the gravitational acceleration; and $t$ is the time. The overbar operator denotes vertically-averaged quantities. Equations (1)−(3) are the continuity, $x$-, and $z$-momentum equations, respectively, while Eqs. (4)−(6) are the moment of continuity, $x$-, and $z$-momentum equations, respectively. Note that $\bar{z}$ is the elevation of the centroid of a section (= $z_b$ + $h$/2). Equations (1)−(6) are weighted-averaged open-channel flow equations, yet not residual, given that ($u$, $w$, $p$) are still general.

In the VAM model [Eqs. (1)−(6)], predictors for the velocity components ($u$, $w$) and the fluid pressure $p$ are required. Steffler and Jin (1993) used finite-element type expansions consisting of a base of functions with a series of coefficients independent of the vertical coordinate. In particular, they expanded $u$ using the first shifted Legendre polynomial, and $w$ and $p$ using the first and second shifted Legendre polynomials, resulting (Steffler and Jin, 1993; Khan and Steffer, 1996a; b):

$$u(x,z,t) = u_0(x,t) + u_1(x,t)\left[2\eta(x,z,t) - 1\right], \tag{7}$$

$$w(x,z,t) = \left[w_b(x,t) + w_2(x,t)4\eta(x,z,t)\right]\left[1-\eta(x,z,t)\right] + w_s(x,t)\eta(x,z,t), \tag{8}$$

$$p(x,z,t) = \left[\rho g h(x,t) + p_1(x,t) + p_2(x,t)4\eta(x,z,t)\right]\left[1-\eta(x,z,t)\right]. \tag{9}$$

Here $u_0$ is the depth-averaged horizontal velocity; $u_1$ is the $x$-velocity at the free surface in excess of $u_0$; $w_2$ is the mid-depth $z$-velocity in excess of the average of the vertical velocities at the bed and free surface levels; $w_b$ and $w_s$ are the vertical velocity at the bed and free surface levels, respectively; $p_1$ is the bed pressure in excess of hydrostatic; $p_2$ is the mid-depth deviation from the linear non-hydrostatic law; and $\eta$ is the dimensionless vertical coordinate [= $(z-z_b)/h$]. The kinematic boundary conditions are expressed as follows (Cantero-Chinchilla et al., 2018; 2020):

$$w_b = \left(u_0 - u_1\right)\frac{\partial z_b}{\partial x}, \tag{10}$$

$$w_s = \frac{\partial h}{\partial t} + \left(u_0 + u_1\right)\frac{\partial z_s}{\partial x}, \tag{11}$$

where $z_s$ is the free surface elevation (= $h + z_b$).

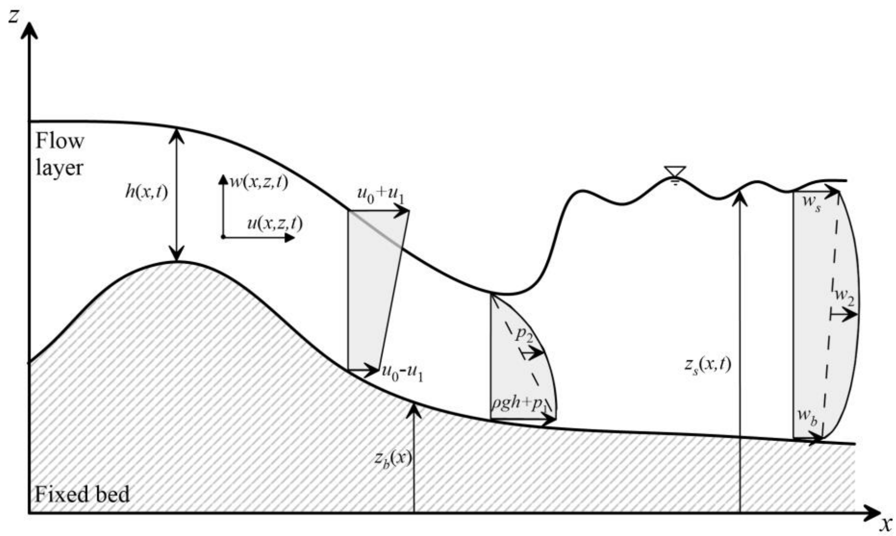


**Fig. 4**. Definition sketch of two-dimensional unsteady turbulent flow.

Inserting Eqs. (7)−(8), which are the trial functions approximating ($u$, $w$, $p$), into Eqs. (1)−(6), the following system of approximate (residual) partial differential equations (PDEs) results:

$$\frac{\partial h}{\partial t}+\frac{\partial q}{\partial x}=0\,, \tag{12}$$

$$\frac{\partial q}{\partial t}+\frac{\partial}{\partial x}\left(g\frac{h^2}{2}+\frac{q^2}{h}\right)=-\frac{\partial}{\partial x}\left(\frac{u_1{}^2 h}{3}+\frac{hp_1}{2\rho}+\frac{2hp_2}{3\rho}-\frac{h\overline{\sigma_x}}{\rho}\right)-gh\frac{\partial z_b}{\partial x}-\frac{p_1}{\rho}\frac{\partial z_b}{\partial x}-\frac{\tau_b}{\rho}\,, \tag{13}$$

$$\frac{\partial h\overline{w}}{\partial t}+\frac{\partial q\overline{w}}{\partial x}=\frac{1}{6}\frac{\partial\left(hu_1 w_*\right)}{\partial x}+\frac{p_1}{\rho}-\frac{\tau_b}{\rho}\frac{\partial z_b}{\partial x}+\frac{1}{\rho}\frac{\partial h\overline{\tau_{xz}}}{\partial x}\,, \tag{14}$$

$$\frac{h}{2}\frac{\partial h}{\partial t}+q\frac{\partial\overline{z}}{\partial x}+\frac{1}{6}\frac{\partial(h^2u_1)}{\partial x}=h\overline{w}\,, \tag{15}$$

$$\begin{aligned}\frac{\partial hu_1}{\partial t}+\frac{\partial qu_1}{\partial x}&=\frac{h}{2\rho}\frac{\partial p_1}{\partial x}+\left(\frac{qu_1}{h}-\frac{p_1}{2\rho}\right)\frac{\partial h}{\partial x}-u_1\frac{\partial q}{\partial x}-\frac{4p_2}{\rho}\frac{\partial\overline{z}}{\partial x}\\&\quad+\frac{6}{\rho}\left(\frac{\tau_b}{2}-\overline{\tau_{xz}}\right)+\frac{6}{\rho h}\left(\frac{\partial h\overline{z\sigma_x}}{\partial x}-\overline{z}\frac{\partial h\overline{\sigma_x}}{\partial x}\right)\end{aligned}\,, \tag{16}$$

$$\frac{\partial}{\partial t}\left(\frac{h^2 w_*}{12}\right)+\frac{\partial}{\partial x}\left(\frac{hqw_*}{12}\right)=\frac{h\bar{w}}{2}\frac{\partial h}{\partial t}+\left(q\bar{w}-\frac{hu_1 w_*}{6}\right)\frac{\partial \bar{z}}{\partial x}+\frac{\partial}{\partial x}\left[\frac{h^2 u_1}{10}\left(\bar{w}+\frac{w_b}{3}+\frac{w_s}{3}\right)\right]$$
$$-h\overline{w^2}-\frac{2hp_2}{3\rho}-\frac{h\tau_b}{2\rho}\frac{\partial z_b}{\partial x}+\frac{h\overline{\sigma_z}}{\rho}-\frac{1}{\rho}\left(\frac{\partial h\overline{z\tau_{xz}}}{\partial x}-\bar{z}\frac{\partial h\overline{\tau_{xz}}}{\partial x}\right),$$

(17)

where $q$ is the discharge per unit width (= $hu_0$); $w_*$ is the vertical velocity difference between the bed and free surface levels (= $w_b - w_s$); $\tau_b$ is the bed shear stress; $\overline{\sigma_x}$ and $\overline{\tau_{xz}}$ are the depth-averaged normal and shear stresses, respectively; and $\overline{w^2}=\bar{w}^2+\frac{1}{12}w_b^2+\frac{1}{12}w_s^2-\frac{1}{6}w_b w_s-\frac{1}{20}\left(2\bar{w}-w_b-w_s\right)^2$. The mean vertical velocity is $\bar{w}$ = $w_b/2 + 2w_2/3 + w_s/2$. Given that the base functions used in the trial solution are used as test functions, the VAM model is a Galerkin-type system of weighted-averaged residual equations (Finlayson and Scriven, 1966). The moment of $x$-momentum Eq. (16) differs from that previously used (Cantero-Chinchilla et al., 2018; Gamero et al., 2020) in that the conservative variable is $hu_1$ instead of $u_1$. This modification was found to increase the numerical robustness of the VAM model when handling dry-wet fronts.

Further, Eqs. (16) and (17) include all turbulent stress terms originating from the weighted-averaging process. Former models in Cantero-Chinchilla et al. (2018) and Gamero et al. (2020) only considered bed-shear effects, thus here, the complete turbulent modeling terms were accounted for in the model equations. The following reactive equation is written based on the kinematic boundary conditions:

$$w_*=\left(\frac{q}{h}-u_1\right)\frac{\partial z_b}{\partial x}+\frac{\partial q}{\partial x}-\left(\frac{q}{h}+u_1\right)\frac{\partial (z_b+h)}{\partial x}. \tag{18}$$

It is a mathematical statement to be verified by the solution at any instant of time. Turbulence closure is required to estimate $\tau_b$, $\overline{\sigma_x}$, $\overline{\sigma_z}$, $\overline{\tau_{xz}}$, $\overline{z\sigma_x}$, and $\overline{z\tau_{xz}}$ in Eqs. (13), (14), (16), and (17). Using an eddy-viscosity approach, these terms read after averaging:

$$\overline{\sigma_x} = 2\rho \frac{\overline{\nu_x}}{h}\left(\frac{\partial q}{\partial x} - u_s\frac{\partial z_s}{\partial x} + u_b\frac{\partial z_b}{\partial x}\right), \tag{19}$$

$$\overline{\sigma_z} = 2\rho \frac{\overline{\nu_z}}{h}\left(w_s - w_b\right), \tag{20}$$

$$\overline{\tau_{xz}} = \frac{\rho\overline{\nu_z}}{h}\left(2u_1 + \frac{\partial h\overline{w}}{\partial x} - w_s\frac{\partial z_s}{\partial x} + w_b\frac{\partial z_b}{\partial x}\right), \tag{21}$$

$$\begin{aligned}\overline{z\sigma_x} = {} & \frac{\rho\overline{\nu_x}h}{3}\left[3\frac{\partial}{\partial x}\left(\frac{q}{h}\right) + \frac{\partial u_1}{\partial x}\right] - \frac{\rho\overline{\nu_x}u_1 z_b}{h}\left(2\frac{\partial h}{\partial x} + 4\frac{\partial z_b}{\partial x}\right) \\ & - \frac{\rho\overline{\nu_x}}{3}\left[4u_1\frac{\partial h}{\partial x} - 6z_b\frac{\partial}{\partial x}\left(\frac{q}{h}\right) + 6u_1\frac{\partial z_b}{\partial x}\right]\end{aligned}, \tag{22}$$

$$\begin{aligned}\overline{z\tau_{xz}} = {} & \rho\overline{\nu_z}u_1 + \frac{2\rho\overline{\nu_z}u_1 z_b}{h} + \frac{\rho\overline{\nu_z}h}{2}\frac{\partial}{\partial x}\left(\overline{w} - \frac{w_b}{6} + \frac{w_s}{6}\right) + \rho\overline{\nu_z}\left(\overline{w} - \frac{w_b}{6} - \frac{5w_s}{6}\right)\frac{\partial h}{\partial x} \\ & + \rho\overline{\nu_z}z_b\frac{\partial\overline{w}}{\partial x} + \rho\overline{\nu_z}\left(\overline{w} - w_s\right)\frac{\partial z_b}{\partial x} + \frac{\rho\overline{\nu_z}z_b}{h}\left(\overline{w} - w_s\right)\frac{\partial h}{\partial x} + \frac{\rho\overline{\nu_z}w_* z_b}{h}\frac{\partial z_b}{\partial x}\end{aligned}, \tag{23}$$

where $\overline{\nu_x}$ and $\overline{\nu_z}$ are the vertically-averaged eddy viscosities in the $x$- and $z$-directions, respectively. In the traditional shallow-water quasi-3D approach, e.g., Rodi (1993), the pressure is assumed to be vertically hydrostatic, with corrections using turbulent stresses based on the depth-averaged horizontal velocity $u_0$. In the present formulation, pressures are dynamic ones, with perturbation parameters $p_1$ and $p_2$, which are corrected in the model equations by the depth-averaged turbulent stresses considering the non-uniform variation of the $u$-velocity with elevation, given by $u_s$, $u_b$ and $u_1$, as well as the vertical velocity $w$ variation, determined by $w_s$, $w_b$ and $w_2$.

Following Ghamry and Steffler (2002a; b), the depth-averaged eddy viscosities are estimated as (Fischer et al., 1979):

$$\overline{\nu_x} = 0.5u_* h, \tag{24}$$

$$\overline{\nu_z} = 0.07 u_* h \,, \tag{25}$$

where $u_*$ is the shear velocity [= $(|\tau_b|/\rho)^{1/2}$]. The bed shear stress is modelled using Manning's formula including vertical velocity effects as follows (Castro-Orgaz and Hager, 2017; Cantero-Chinchilla et al., 2018; 2020):

$$\tau_b = \rho g \frac{n^2 \left( u_b{}^2 + w_b{}^2 \right)}{h^{1/3}} \,, \tag{26}$$

where $n$ is the Manning's roughness coefficient.

### *3.2 Numerical modeling and Software development*

The software development entails the solution of the turbulent VAM model [Eqs. (12)−(17)] through numerical techniques, given that an analytical solution of the system of PDEs equations is unknown. A semi-implicit finite volume (FV)-finite difference (FD) scheme is developed based on former works (Cantero-Chinchilla et al., 2018; 2020; Gamero et al., 2020). Former solvers were prone to numerical instabilities if shocks or moving hydraulic jumps were progressively developed in the solution, causing the solution failure in some cases. Therefore, a special feature of the new solver constructed is its ability for handling the formation of shocks with robustness, as described below.

The VAM model is in matrix form:

$$\frac{\partial \mathbf{U}}{\partial t} + \frac{\partial \mathbf{F}}{\partial x} = \mathbf{S}_o + \mathbf{S}_\tau \,, \tag{27}$$

where vectors **U**, **F** and **S** enclose, respectively, the flow conservative variables, fluxes and source terms:

$$\mathbf{U}=\begin{bmatrix} h \\ q \\ h\bar{w} \\ hu_1 \\ \dfrac{h^2 w_*}{12} \end{bmatrix}, \mathbf{F}=\begin{bmatrix} q \\ \dfrac{q^2}{h}+g\dfrac{h^2}{2} \\ q\bar{w} \\ qu_1 \\ \dfrac{hqw_*}{12} \end{bmatrix}, \tag{28}$$

$$\mathbf{S}_o=\begin{bmatrix} 0 \\ -\dfrac{\partial}{\partial x}\left(\dfrac{u_1{}^2 h}{3}+\dfrac{hp_1}{2\rho}+\dfrac{2hp_2}{3\rho}\right)-gh\dfrac{\partial z_b}{\partial x}-\dfrac{p_1}{\rho}\dfrac{\partial z_b}{\partial x} \\ \dfrac{1}{6}\dfrac{\partial\left(hu_1 w_*\right)}{\partial x}+\dfrac{p_1}{\rho} \\ \dfrac{h}{2\rho}\dfrac{\partial p_1}{\partial x}+\left(\dfrac{qu_1}{h}-\dfrac{p_1}{2\rho}\right)\dfrac{\partial h}{\partial x}-u_1\dfrac{\partial q}{\partial x}-\dfrac{4p_2}{\rho}\dfrac{\partial \bar{z}}{\partial x} \\ \left[-\dfrac{h\bar{w}}{2}\dfrac{\partial q}{\partial x}+\left[q\bar{w}-\dfrac{hu_1 w_*}{6}\right]\dfrac{\partial \bar{z}}{\partial x} \right. \\ \left. +\dfrac{\partial}{\partial x}\left[\dfrac{h^2 u_1}{10}\left(\bar{w}+\dfrac{w_b}{3}+\dfrac{w_s}{3}\right)\right]-h\overline{w^2}-\dfrac{2hp_2}{3\rho}\right] \end{bmatrix},$$

$$\mathbf{S}_\tau=\begin{bmatrix} 0 \\ +\dfrac{1}{\rho}\dfrac{\partial h\overline{\sigma_x}}{\partial x}-\dfrac{\tau_b}{\rho} \\ -\dfrac{\tau_b}{\rho}\dfrac{\partial z_b}{\partial x}+\dfrac{1}{\rho}\dfrac{\partial h\overline{\tau_{xz}}}{\partial x} \\ +\dfrac{6}{\rho}\left(\dfrac{\tau_b}{2}-\overline{\tau_{xz}}\right)+\dfrac{6}{\rho h}\left(\dfrac{\partial h\overline{z\sigma_x}}{\partial x}-\bar{z}\dfrac{\partial h\overline{\sigma_x}}{\partial x}\right) \\ -\dfrac{h\tau_b}{2\rho}\dfrac{\partial z_b}{\partial x}+\dfrac{h\overline{\sigma_z}}{\rho}-\dfrac{1}{\rho}\left(\dfrac{\partial h\overline{z\tau_{xz}}}{\partial x}-\bar{z}\dfrac{\partial h\overline{\tau_{xz}}}{\partial x}\right) \end{bmatrix}, \tag{29}$$

The subscripts $o$ and $\tau$ refer to the inviscid and the turbulent stress source terms, respectively. Note that only transport Eqs. (12)–(14), (16), and (17) are contained into Eq. (27) which, together with the reactive Eqs. (15) and Eq. (18), conforms the VAM model.

This shallow-water VAM model is more complex than the Saint Venant equations, but its features are significantly better. It may be noted that the RANS equations are simpler in its formulation. However, the computational cost of a full 3D approach is still high at a river scale (Katopodes 2019), involving the determination of the free surface boundary using the volume of fluid or level set methods. In contrast, the position of the free surface is directly resolved in this depth-averaged formulation. Note that the VAM equations look complex given their long source terms [see Eqs. (29)], but the architecture of the equations is similar to that of the standard shallow water equations [see Eq. (27)]. The solution of this model is vectorized in the present code, such that implementation is easy.

The semi-implicit FV-FD scheme follows a splitting approach in two stages: (i) a hyperbolic step and (ii) an elliptical step.

Dividing the $x$-$t$ plane into quadrilateral finite volume cells of dimensions $\Delta x \times \Delta t$, in the hyperbolic step an intermediate solution is obtained from the homogenous part of Eq. (27) using a Godunov-type finite-volume scheme (Toro, 2001; 2009):

$$\hat{\mathbf{U}}_i = \mathbf{U}_i^k - \frac{\Delta t}{\Delta x}\left(\mathbf{F}_{i+1/2} - \mathbf{F}_{i-1/2}\right). \tag{30}$$

In Eq. (30), **U** and **F** are space- and time-averaged vectors; $i$ is the cell index; $k$ is a time index; $\Delta x$ is the $x$-dimension of the control volume; $\Delta t$ is the $t$-dimension of the control volume. The indices $i \pm 1/2$ refer to the control volume interfaces between cells $i$ and $i \pm 1$. The numerical flux $\mathbf{F}_{i+1/2}$ is determined using the approximate Riemann solver HLLC (Toro, 2001; 2009). Note that contact waves are accounted for in the solution of Eq. (30), as those described by the conservative variables $h\overline{w}$, $hu_1$ and $\frac{1}{12}h^2 w_*$. Here, the MUSCL–Hancock scheme (Toro, 2001; 2009), which is the second-order accurate in space and time, is applied to reconstruct **U**. This produces more efficient and robust computations than former solvers based on 4th-order accurate reconstructions (Cantero-Chinchilla et al., 2018; Gamero et al., 2020). Besides, to avoid unphysical numerical flux during the reconstruction of the flow depth over uneven topography, the weighted surface-depth gradient method (WSDGM) (Aureli et al., 2008) is used, where at the cell interfaces, the water depth is determined as an average of the values obtained reconstructing the free surface and the water depth independently. Dry cells are identified as those where the flow depth $h$ is below a prescribed tolerance, which is adopted as $h_{tol} = 10^{-6}$ in this work. At a dry cell all variables are reset to zero.

In the elliptical step, the solution is updated in two stages using finite-difference schemes. The first stage of the elliptical step is called inviscid finite-difference step, which is designed to incorporate the non-hydrostatic pressure effects into the solution using an implicit scheme. Using the backward Euler formula, the system of equations to solve is in compact form:

$$\tilde{\mathbf{U}}_i = \hat{\mathbf{U}}_i + \Delta t\left[\mathbf{S}_0\left(\tilde{\mathbf{U}}_i\right)\right]. \tag{31}$$

The implicit system of equations described by Eq. (31) is coupled to the reactive Eqs. (15) and (18) and solved using a Newton–Raphson (NR) method to obtain $\tilde{\mathbf{U}}$. The spatial derivates in Eqs. (15), (18) and (31) are discretized using second-order central finite differences. If shocks are formed in any portion of the computational domain, the gradients of some of the flow variables may reach large values. These may result in numerical instabilities. A new special method for handling shock development is presented in the next section. Here, it is assumed that the solution is smooth throughout the computational domain.

Setting appropriate initial values for the unknown variables ($q$, $u_1$, $p_1$, $p_2$, $\bar{w}$ and $w_*$) a vector of residuals $\mathbf{r} = \tilde{\mathbf{U}}_i^m - \hat{\mathbf{U}}_i - \Delta t\left[\mathbf{S}_0\left(\tilde{\mathbf{U}}_i^m\right)\right]$ is defined, where $m$ is a recursion index. Residuals are reduced by computing an analytical Jacobian $\mathbf{J}$ for the unknown variables at nodes $i-1$, $i$ and $i+1$, yielding a $6N\times6N$ diagonal matrix formed by 108 partial derivates per cell, where $N$ is the number of cells. The matrix equation $\mathbf{r} = \mathbf{J} \times \mathbf{d}\tilde{\mathbf{U}}_i$ is solved at each iteration of the solution, where $\mathbf{d}\tilde{\mathbf{U}}_i$ is the vector of corrections. Should a dry cell be detected, the corresponding residuals are set to zero [all except Eq. (13), which is not updated]. Once $\mathbf{d}\tilde{\mathbf{U}}_i$ is determined through the pertinent matrix inversion, it is employed to update the solution vector, i.e., $\tilde{\mathbf{U}}_i^{m+1} = \tilde{\mathbf{U}}_i^m + \mathbf{d}\tilde{\mathbf{U}}_i$, where $\tilde{\mathbf{U}}_i^{m+1}$ is the updated solution. This process is repeated in the NR method at every time step until convergence. The convergence criterion suggested by Khan and Steffler (1996a) is implemented, stopping the iterations if the mean relative error is below a prescribed tolerance, settled as $10^{-6}$ in this work. To save computational cost, at each time step **J** is frozen, i.e., computed at the start of the loop (Cantero-Chinchilla et al., 2018; 2020).

The second stage of the elliptical step consists in an explicit update of the solution vector $\tilde{\mathbf{U}}$ by incorporating the turbulent source terms, $\mathbf{S}_\tau$, resulting using the forward Euler formula:

$$\mathbf{U}_i^{k+1} = \tilde{\mathbf{U}}_i + \Delta t \left[ \mathbf{S}_\tau \left( \tilde{\mathbf{U}}_i \right) \right]. \qquad (32)$$

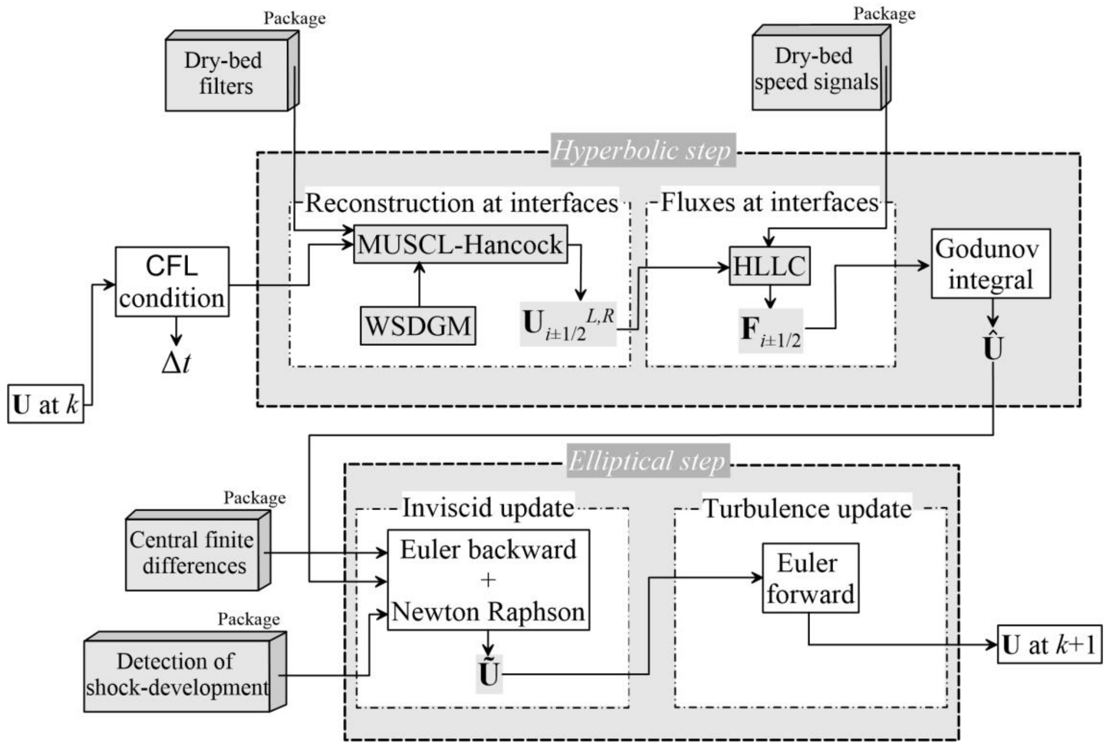


**Fig. 5**. Flow chart of the numerical scheme.

Figure 5 shows a flow chart of the numerical sequence described above, which is followed in every time step. The Courant–Friedrichs–Lewy (CFL) condition is used to compute $\Delta t$ thus ensuring numerical stability of the hybrid FV–FD scheme, i.e., $\Delta t = (\mathrm{CFL}\cdot\Delta x)/(|u_0 + c|)$ where $c = (gh)^{1/2}$ is the long wave celerity and CFL $\leq 0.5$ by numerical experimentation. Although the numerical scheme is stable for CFL $\leq 0.5$, we generally used CFL = 0.2 in the computations presented to reduce truncation errors in the output solutions.

### *3.2.1 Detection of shock-development*

During wave propagation simulations, the VAM model has the ability to generate shocks or moving hydraulic jumps, which are mathematically represented as a weak solution of the system of conservations laws involving discontinuities in one or some of the flow variables, namely $q$, $z_s$, $u_1$, $\overline{w}$, $p_1$ and $p_2$. The shocks or discontinuity-like portions of the solutions are generated in the hyperbolic solver of the software. When these portions of the solution are processed by the elliptic solver, the computation of the gradients of the flow variables near such steep fronts produces quantities with an extremely large magnitude, producing numerical instabilities when the Jacobian matrix is formed and inverted, if feasible. The pathological computations described are especially dramatic if one attempts to make a mesh-refinement study of the solution, which is mandatory when presenting numerical solutions. If $\Delta x$ is progressively reduced to get mesh-independent results, the hyperbolic solver produces sharper discontinuities, given the increased resolution. Processing of these solutions by the elliptic solver encounters not only shaper shocks, but also a smaller $\Delta x$, thus much higher gradients, thereby guaranteeing solution crashing. Previous solvers (Cantero-Chinchilla et al., 2018; Gamero et al., 2020) were found to suffer from this issue while dealing with the moving hydraulic jumps experimentally generated in this research, thus a special solver for robust handling of shocks was developed as follows.

The following gradients of the flow variables are used as shock-development sensors:

$$\frac{\partial z_s}{\partial x},\ \frac{\partial}{\partial x}\left(\frac{q^2}{gh^2}\right),\ \frac{\partial}{\partial x}\left(\frac{u_1^2}{g}\right),\ \frac{\partial}{\partial x}\left(\frac{\overline{w}^2}{g}\right),\ \frac{\partial}{\partial x}\left(\frac{p_1}{\gamma}\right),\ \frac{\partial}{\partial x}\left(\frac{p_2}{\gamma}\right), \tag{33}$$

thereby permitting to detect formation of shocks in the output of the hyperbolic solver. A threshold value for the gradients $\Phi_{thr}$ is defined, which is set at 75º by numerical experimentation for meshes involving $\Delta x \leq 0.01$ m. A shock is considered formed in the output of any of the flow variables if the corresponding gradient is above this threshold. If this occurs in a cell, the non-hydrostatic flow variables are reset to zero in a bandwidth equal to the stencil used to compute dispersive terms, e.g., $2\Delta x$. This process eliminates the gradients near sharp discontinuities and permits a robust numerical handling. At the initial stage of the dam-break flow generation this process is not applied, given that the initial condition is itself a discontinuity. Thus, the shock-development detection is applied for $t > t_0$, where $t_0$ is the hydrodynamic time scale [= $(h_u/g)^{1/2}$] (Wu and Wang, 2007), which is of the order of the gate opening time in the experiments.

### 3.2.2 Boundary conditions in dam-break wave experiments

To mimic numerically the experiments conducted in the flume, boundary conditions must be modelled with accuracy. The boundary conditions are incorporated in the mathematical model using ghost cells at boundaries. Computational cells are from $i$ = 1 to $i$ = $N$. At the tailwater section of the flume, the closed gate is modeled as a reflective boundary condition, i.e., $h_{N+2}=h_{N+1}=h_N$ and $q_{N+2}=q_{N+1}=-q_N$ (Toro, 2001) with the remaining variables in the VAM model reset to zero. This was found to reproduce well the experimental observations. At the upstream end of the flume, a transmissive boundary condition is implemented for all variables but except the flow depth, i.e., $(q,u_1,p_1,p_2,\overline{w},w_*)_{-1}=(q,u_1,p_1,p_2,\overline{w},w_*)_2$ and $(q,u_1,p_1,p_2,\overline{w},w_*)_0=(q,u_1,p_1,p_2,\overline{w},w_*)_1$. The flow depth in the cells $i = -1$ and $i = 0$ is computed by setting energy conservation in the water tank using the experimentally determined time-variation of $h_{uw}$:

$$E_{-1} = E_0 = h_{uw} = \frac{1}{100}\left(0.0015t^4 - 0.032t^3 + 0.1656t^2 - 0.2503t + 0.0393\right) + h_1, \quad (34)$$

Here $E$ is the specific energy. Flow depths are thus obtained by analytical inversion of the specific energy diagram as follows:

$$\begin{bmatrix} h_{-1} \\ h_0 \end{bmatrix} = \begin{bmatrix} E_{-1}\left[\frac{1}{3}+\frac{2}{3}\cos\left(\frac{\gamma_{-1}}{3}\right)\right] \\ E_0\left[\frac{1}{3}+\frac{2}{3}\cos\left(\frac{\gamma_0}{3}\right)\right] \end{bmatrix}, \quad (35)$$

where:

$$\begin{bmatrix} \gamma_{-1} \\ \gamma_0 \end{bmatrix} = \begin{bmatrix} \operatorname{arcos}\left[1-\dfrac{27}{4}\left(\dfrac{E_{-1}}{h_{c,-1}}\right)^{-3}\right] \\ \operatorname{arcos}\left[1-\dfrac{27}{4}\left(\dfrac{E_0}{h_{c,0}}\right)^{-3}\right] \end{bmatrix}, \tag{36}$$

$$\begin{bmatrix} h_{c,-1} \\ h_{c,0} \end{bmatrix} = \begin{bmatrix} \left(\dfrac{q_2{}^2}{g}\right)^{1/3} \\ \left(\dfrac{q_1{}^2}{g}\right)^{1/3} \end{bmatrix}. \tag{34}$$

The flow depth computed using Eq. (35) corresponds to the subcritical root of the specific energy diagram (Castro-Orgaz and Hager, 2019).

The inviscid part of the VAM equations is not new in the solver presented, but the model equations here include the turbulent stresses. The numerical solver is new, and includes important capabilities not available in a previous model by Cantero-Chinchilla et al. (2018):

1. Inclusion of turbulence by an eddy-viscosity approach.

2. Inclusion of a new module for shock detection in the elliptic step, allowing mesh refinement.

3. Use of the robust MUSCL-Hancock scheme in the hyperbolic step.

4. Dry bed treatment allowed.

The old VAM-2018 model failed during trials to run it for the new experimental conditions presented, due to the formation of hydraulic jumps and the dry bed zones, resulting in a collapse in computations.

## 4. Results

### *4.1 Benchmark numerical tests*

Several challenging benchmark tests are selected in this section to evaluate the ability of the VAM model to deal with discontinuous topography, to grant the C-property and to tackle dry-wet unsteady fronts. First, a tidal wave test over a submerged rectangular step by Bermudez and Vázquez (1994) is used to validate the capability of the model on dealing with discontinuous topography (Zhou et al., 2002; Liang and Marche, 2009). The tidal wave is designed to occur in a 1500-m-long frictionless channel with asymptotic analytical flow solution as follows:

$$h = 20 - z_b - 4\sin\left[\pi\left(\frac{4t}{86400} + \frac{1}{2}\right)\right], \tag{35}$$

$$u_0 = \frac{(x-L)\pi}{5400h}\cos\left[\pi\left(\frac{4t}{86400} + \frac{1}{2}\right)\right], \tag{36}$$

where $L$ = 1500 m. The bed profile is:

$$z_b = \begin{cases} 8 & \text{if } \quad |x - 750| \le 187.5, \\ 0 & \text{otherwise.} \end{cases} \tag{37}$$

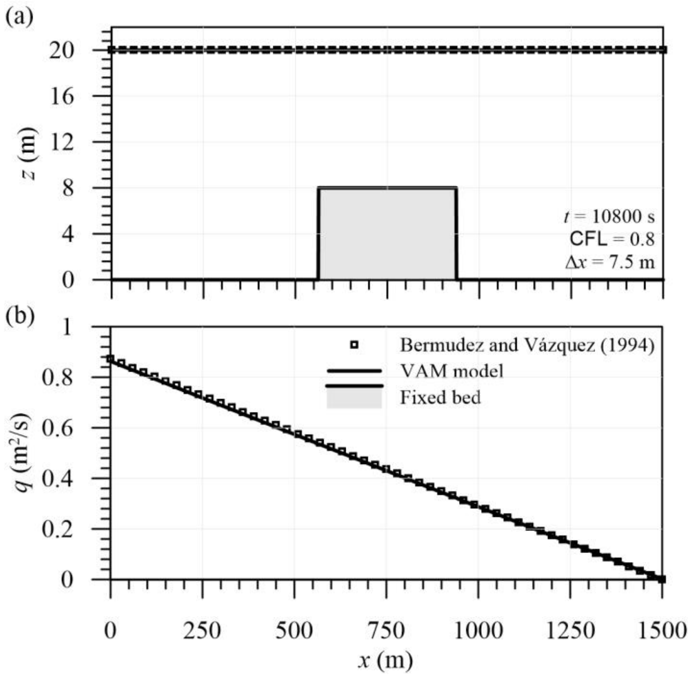


**Fig. 6**. Bed discontinuity test using the analytical solutions for tidal waves over a submerged vertical step by Bermudez and Vázquez (1994) in comparison with VAM model results at $t$ = 10800 s for: (a) flow depth and (b) unit discharge.

The test is conducted herein using $\Delta x$ = 7.5 m and CFL = 0.8 until $t$ = 10800 s is reached. Equations (38) and (39) are used to set the initial conditions, i.e., substituting $t$ = 0 s, while Eq. (38) is used to impose the inlet boundary condition at $x$ = 0 m. The right end of the channel is modelled using a reflective, closed boundary condition. VAM model results for this test are shown in Fig. 6, depicting an excellent agreement with the analytical solution in both water surface (Fig. 6a) and unit discharge (Fig. 6b) predictions at $t$ = 10800 s, where bed discontinuities did not impact the numerical solution.

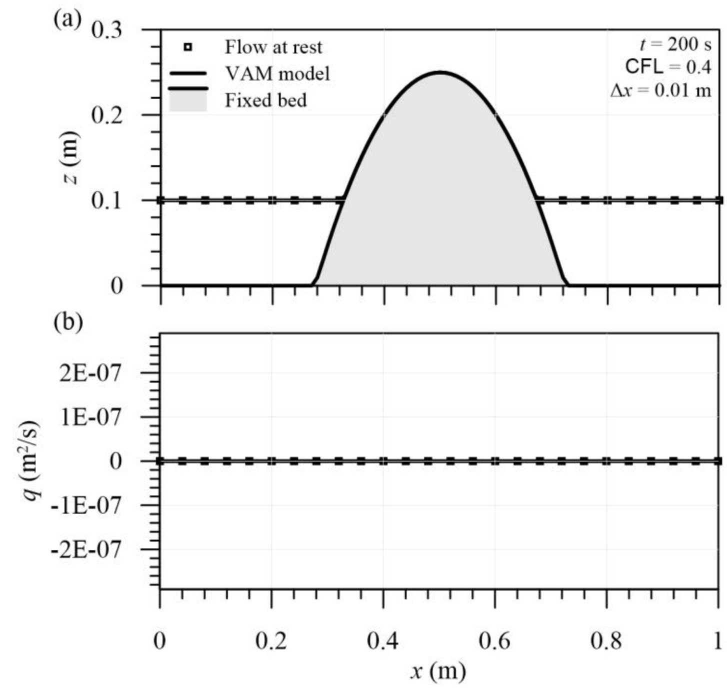


**Fig. 7**. Preservation of still water surface at a surface-piercing hump test by Liang and Marche (2009) in comparison with VAM model results at $t$ = 200 s for: (a) flow depth and (ii) unit discharge.

Second, a still water test at a surface-piercing hump (Liang and Marche, 2009), i.e., with dry-wet interfaces, is selected to evaluate the preservation of C-property by the proposed VAM model. For this test, the channel is 1-m-long and frictionless, with the surface-piercing hump defined by:

$$z_b = \max\left[0, 0.25 - 5\left(x - 0.5\right)^2\right], \tag{38}$$

where the flow is at rest with maximum depth of 0.1 m. The test is conducted herein using $\Delta x$ = 0.01 m and CFL = 0.4 until $t$ = 200 s. Figure 7 shows the VAM model results for the free surface and the unit discharge after 200 s of computation, where the agreement with the static solution at rest is excellent.

Finally, the analytic solutions by Thacker (1981) for an oscillating shoreline in a parabolic bowl are used to evaluate the ability of the proposed VAM model to tackle dry-wet fronts in movement over a non-uniform slope (Liang and Marche, 2009; Lai and Khan, 2018). The analytical solutions for the flow depth and the unit discharge in a rectangular channel with parabolic bed profile are (Thacker, 1981; Lai and Khan, 2018):

$$z_s = \max\left[z_b, -\frac{B^2\cos(2\omega t) + B^2 + 4Bx\omega\cos(\omega t)}{4g}\right] \tag{39}$$

$$q = \max\left[0, (z_s - z_b)\right] B\sin(\omega t) \tag{40}$$

with

$$\omega = \frac{2\pi}{T} = \frac{\sqrt{2gh_0}}{l_0} \tag{41}$$

where $T$ is the period, $\omega$ is the frequency, $B$ is a speed parameter, and $h_0$ and $l_0$ are definition parameter for the parabolic bed, which is $z_b = h_0[(x/l_0)^2 - 1]$. This test is conducted herein using $\Delta x = 0.01$ m, CFL = 0.4, $h_0 = 10$ m, $l_0 = 600$ m and $B = 5$ m/s until $t = T = 269$ s. The domain extended to $x \in [-1000, 1000]$ m, thus yielding the boundaries unaffected by the flow during the computation. Figure 8 shows the VAM model results for flow depth and unit discharge at three different instants: (i) at $t = T/2$ when the flow reaches its highest position to the right (Figs. 8a and b), (ii) at $t = 3T/4$ when the flow passes through the horizontal position advancing towards the left end (Figs. 8c and d), and (iii) at $t = T$ when the flow reaches its highest position to the left (Figs. 8e and f). The VAM model results show an accurate agreement with the analytical solutions at all computed instants, where the moving dry-bed fronts are accurately tackled validating the wetting-drying algorithm in the model.

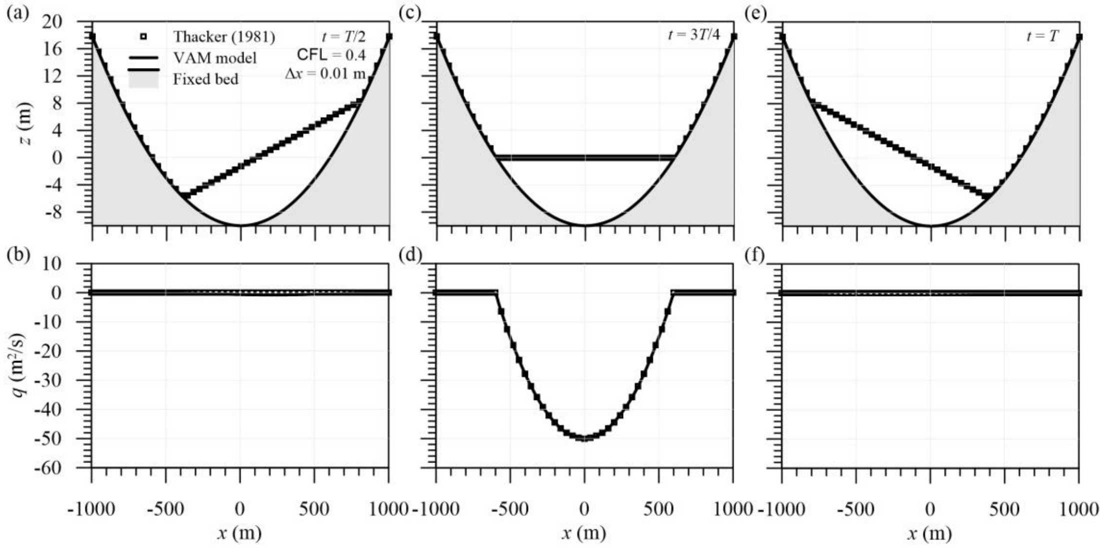


**Fig. 8**. Evolution of shorelines over a frictionless parabolic bowl test by Thacker (1981) in comparison with VAM model results for flow depth and unit discharge at different instants: $t = T/2$ (a)-(b), $t = 3T/4$ (c)-(d), and $t = T$ (e)-(f).

### *4.2 Lee-side waves*

The ability of the VAM model on reproducing the challenging experimental flow tests produced in this work is evaluated is this section. To this end, all tests described in section 2.2, Table 1, were simulated using $\Delta x = 0.01$ m, CFL = 0.2 and $n = 0.01$ ms$^{-1/3}$. The numerical tests were repeated using CFL = 0.1, thereby confirming mesh-independence of the numerical results. The VAM model results for the tests 1−4 are shown in Figs. 10−13, respectively, where four instants were selected to illustrate the main phenomena in the transformation of waves in the test series: (i) initial stages of dam-break flow generation at $t = 1$ s or 2 s, (ii) wave reflection at the right end of the flume at $t = 5$ s, (iii) wave interaction with the unsteady hydraulic jump formed at the toe of the obstacle at $t = 8$ s, and (iv) reflected and diffracted waves produced after the incoming surge surpassed the obstacle, at $t = 12$ s.

Figure 9 shows the VAM model results in comparison with the experimental data for test 1, where $r = 0.397$, as well as the Saint Venant equations (dSV) model predictions. In test 1, the non-linearity effects are the highest among the test series, also depicting the most challenging unsteady hydraulic jump formed at the toe of the lee slope of the obstacle. The VAM model accurately predicts the initial stages of the dam-break flow as shown in Fig. 9a, which represents the experimental data at $t = 1$ s. The amplitude of the leading broken wave (Fig. 9a, $x = 10.7$ m) is, however, slightly overestimated. While the VAM model is able to accurately approximate the advancing bore position, the dSV model anticipates its location (Fig. 10a, $x = 10.9$ m). Figure 9b represents the experimental data at $t = 5$ s, after the flow reflection at the right end of the flume. The VAM model results show excellent agreement with the experimental data of the reflected train of waves, the hydraulic jump profile, and the drawdown in the upstream water level as the rarefaction wave advances backwards. The dSV model, however, fails to approximate the reflected train of waves, which is attributed to the lack of dispersive terms. The experimental data at $t = 8$ s is represented in Fig. 9c, depicting the interaction between the reflected train of waves and the moving-forward hydraulic jump at the toe of the obstacle. While the effect of the rarefaction wave as well as the reflected train of waves near the flume end are accurately predicted by the VAM model, discrepancies between the model results and the data are found in both the interaction zone and the hydraulic jump, with a peak predicted by the VAM model not observed in the experiments. The VAM model computed the dynamic pressures in an elliptic step by solving the relevant system of equations iteratively. In the vicinity of a hydraulic jump, the perturbation parameters determining the pressure field $p_1$ and $p_2$ are subjected to abrupt changes, and thus inviscid pressure peaks are generated as solution in the elliptic step, thereby resulting also in abrupt wave peaks in the free surface profile at the next time step. Turbulence is incorporated in the model using an eddy-viscosity approach. The mismatch of computations and predictions at $t = 8$ s indicates that the modeled turbulent stresses are not strong enough to suppress the effect of the inviscid pressure peaks at some time instants. The approximated turbulence closure in the proposed VAM model, which incorporates the bed-dominating turbulence approximation for eddy-viscosity by Ghamry and Steffler

(2002a; b), may be the origin of this misprediction. A more sophisticated approach including turbulence diffusion and production may be needed to characterize the interaction zone of the hydraulic jump and the reflected wave. Finally, Fig. 9d shows the experimental data at $t$ = 12 s in comparison with VAM and dSV model results. Overall, the VAM model is capable of predicting most of the reflected and diffracted waves, leading to some mispredictions especially for the leading wave amplitude in the reflected bore. These discrepancies may stem from the misprediction of the flow interaction around $t$ = 8 s (Fig. 9c), but are unrelated to stability issues of the model. Despite this weakness, the turbulent VAM model prediction of the experimental data by test 1 is accurate as compared to that of the dSV model. $L$ and $L^2$ norms for VAM and dSV simulations are given in Table 2.

**Table 2.** $L$ and $L^2$ norms for VAM and dSV simulations in Fig. 9

| | $t$ = 1 s | | $t$ = 5 s | | $t$ = 8 s | | $t$ = 12 s | |
|---|---|---|---|---|---|---|---|---|
| | **VAM** | **dSV** | **VAM** | **dSV** | **VAM** | **dSV** | **VAM** | **dSV** |
| $L$(m) | 0.563 | 0.728 | 1.573 | 1.843 | 1.604 | 1.841 | 1.105 | 1.468 |
| $L^2$(m) | 0.092 | 0.107 | 0.369 | 0.380 | 0.265 | 0.271 | 0.140 | 0.182 |

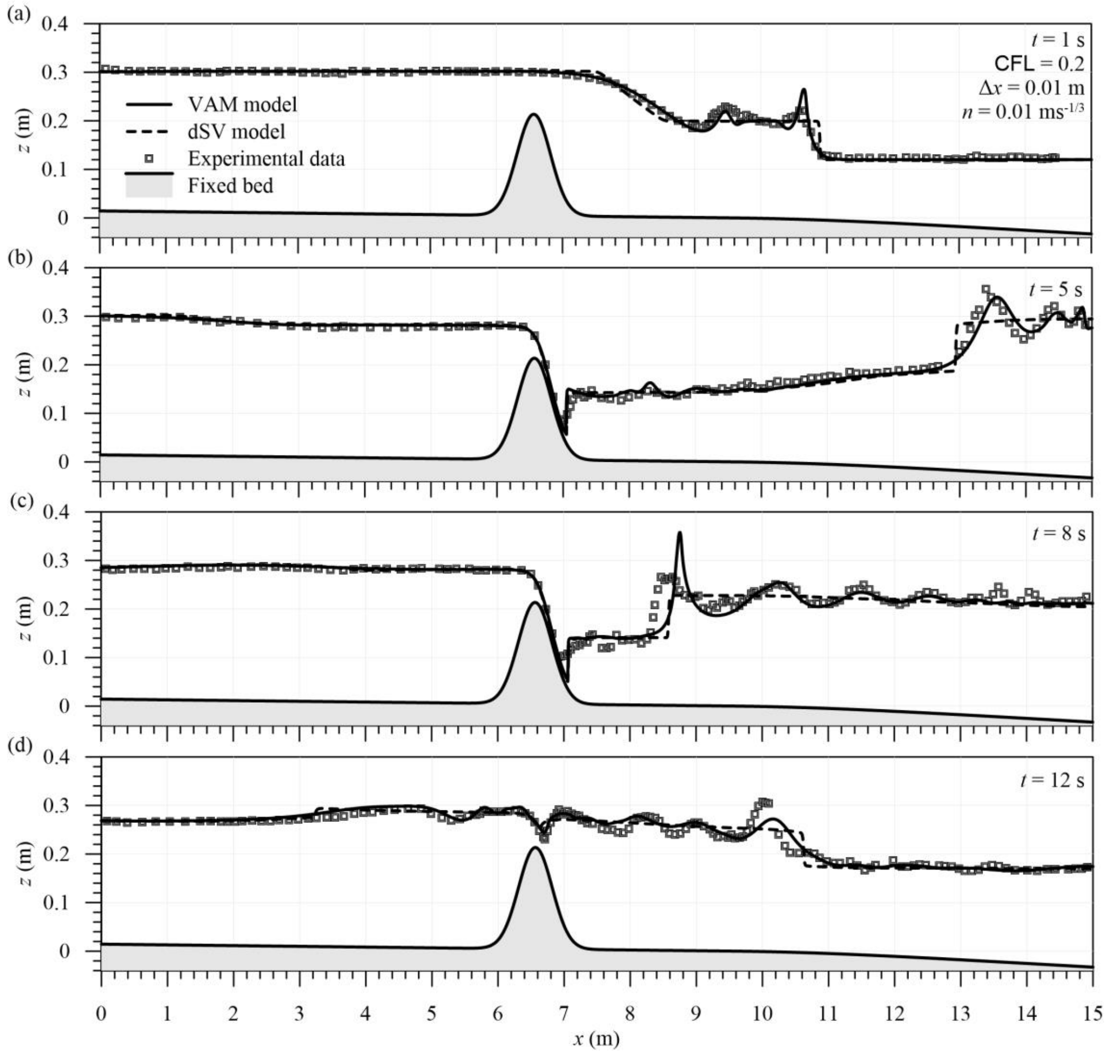


**Fig. 9**. VAM model results for test 1 in comparison with the experimental data and the dSV model predictions at: (a) $t$ = 1 s, (b) $t$ = 5 s, (c) $t$ = 8 s, and (d) $t$ = 12 s.

Figure 10 shows the VAM model results in comparison with the experimental data extracted for test 2, where $r$ = 0.6, as well as the dSV model predictions. In test 2, the non-linear effects in the advancing bore are expected to decrease as compared to those given by test 1, thus leading to a non-breaking bore at the initial stages of the dam-break flow as observed during the experimentation. In addition, during the test, the unsteady hydraulic jump was observed to develop a shorter front than that by test 1.

Figure 10a shows the experimental data at $t = 2$ s, i.e., the dam-break flow right after the initial stages, in comparison with the VAM and dSV model results. Here, the VAM model provides the results in excellent agreement with the experimental data but for the leading wave amplitude (Fig. 10a, $x = 12$ m), it is slightly underestimated. In Fig. 10b, the experimental data at $t = 5$ s is shown, where the dam-break flow has already been reflected at the right end of the flume and the hydraulic jump at the toe of the obstacle begins to develop, in comparison with the results by both models. While the dSV model less predicts the reflected train of waves, the VAM model is able to accurately approximate the experimental data at $t = 5$ s; however, it leads to an overestimation of the zone of development of the hydraulic jump at the toe of the obstacle. Note that the latter referred zone is mainly turbulence dominated and, thus, the accuracy of VAM model results may suffer from the approximate turbulence closure considered in this work. The overestimation of the initial stages of the hydraulic jump is also evident in Fig. 10c, where the experimental data at $t = 8$ s is plotted against the VAM and dSV model results. Albeit the two leading waves at the front of the reflected bore are accurately approximated by the VAM model, the amplitude and phase of the train of waves are slightly misinterpreted. However, the impact of this underestimation in the train of waves at $t = 8$ s is minimal on the approximation of the subsequent test data, as shown in Fig. 10d for the experimental data at $t = 12$ s in comparison with both models results. The results by the VAM model are overall satisfactory for $t = 12$ s, where the major discrepancies with respect to the experimental data focus on the amplitude of the train of waves upstream and downstream the obstacle. $L$ and $L^2$ norms for VAM and dSV simulations are given in Table 3.

**Table 3.** $L$ and $L^2$ norms for VAM and dSV simulations in Fig. 10

| | $t = 2$ s | | $t = 5$ s | | $t = 8$ s | | $t = 12$ s | |
|---|---|---|---|---|---|---|---|---|
| | **VAM** | **dSV** | **VAM** | **dSV** | **VAM** | **dSV** | **VAM** | **dSV** |
| $L$(m) | 0.784 | 1.086 | 1.257 | 1.776 | 1.723 | 2.357 | 1.333 | 1.800 |
| $L^2$(m) | 0.092 | 0.149 | 0.140 | 0.209 | 0.189 | 0.256 | 0.135 | 0.172 |

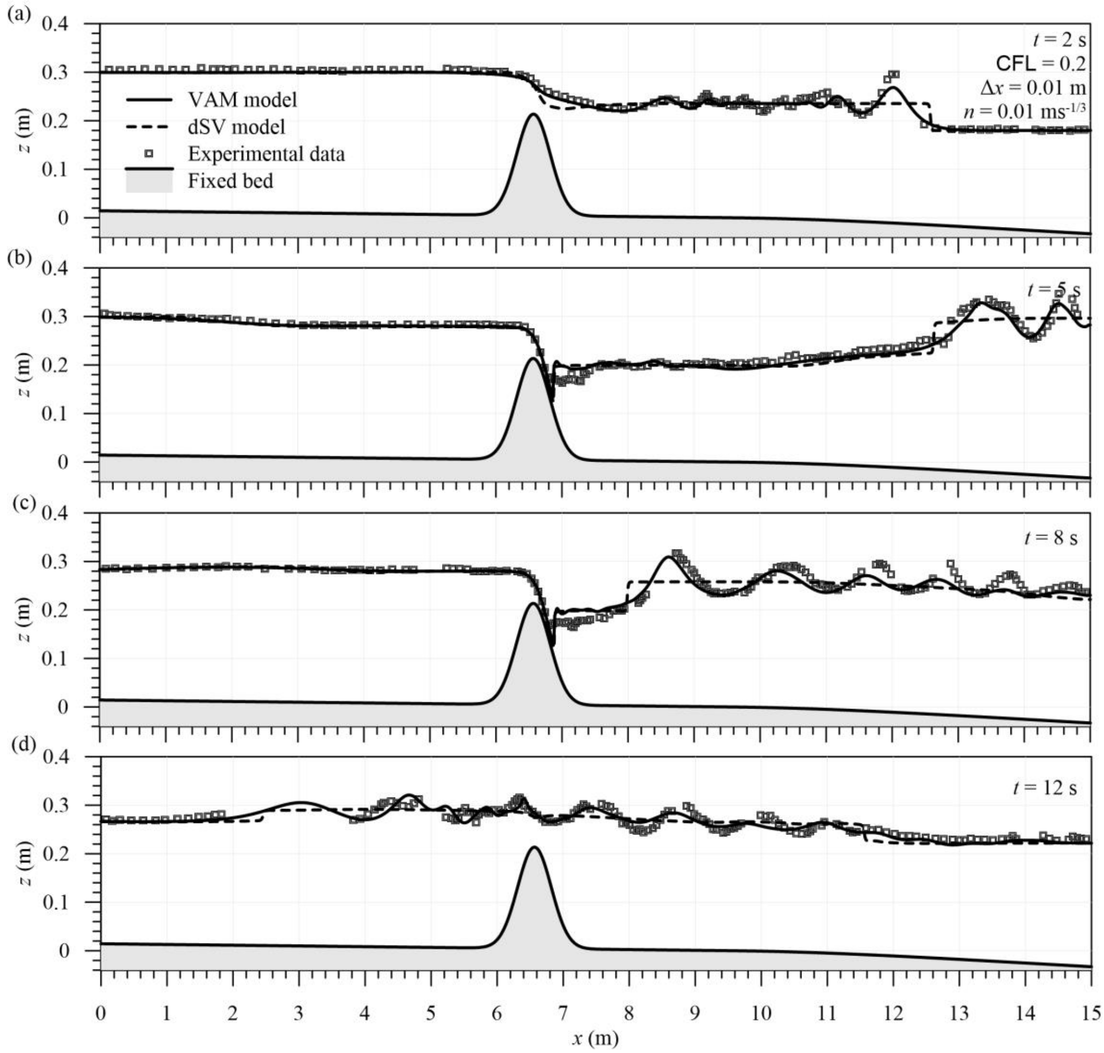


**Fig. 10**. VAM model results for test 2 in comparison with the experimental data and the dSV model predictions at: (a) $t$ = 2 s, (b) $t$ = 5 s, (c) $t$ = 8 s, and (d) $t$ = 12 s.

Figure 11 shows the VAM model results in comparison with the experimental data extracted for test 3, where $r$ = 0.8, as well as the dSV model predictions. In test 3, the wave non-linearity is minimum as the dam-break depth ratio approaches unity. During the experiments, the unsteady hydraulic jump at the toe of the obstacle was observed to be very close to the crest. The experimental data at $t$ = 2 s is shown in Fig. 11a, where the VAM model provides a good approximation of the data in contrast to the prediction by the dSV model, which not only anticipates the bore position and mispredicts the train of waves but also depicts a fictitious, incipient hydraulic jump at the lee slope of the obstacle. It is noteworthy that during the experimentation in test 3, a notable surface water splash was observed after the sluice gate opening, thus contaminating the experimental data in the subsequent time instants. In consequence, the experimental free surface was hardly tracked at $t < 2$ s and, therefore, those time instants are not shown in Fig. 11. In Fig. 11b, the experimental data at $t = 5$ s is shown. Here, the VAM model is demonstrated to be able to predict all the data. However, hydraulic jump and the amplitude of the leading reflected wave are slightly overestimated and underestimated, respectively. The experimental data at $t = 8$ s is presented in Fig. 11c, where the VAM model accurately approximates the experimental data of the reflected train of waves before they encounter back the obstacle. Figure 11d presents the experimental data at $t = 12$ s, after the transformation of the reflected dam-break waves and the interaction back with the obstacle. In line with the results for the experimental data at $t = 12$ s in the experiments 1 and 2, the VAM model provides a fair approximation of the experimental data, where only major mispredictions are found in the phase of the train of waves upstream the obstacle. $L$ and $L^2$ norms for VAM and dSV simulations are given in Table 4.

**Table 4.** $L$ and $L^2$ norms for VAM and dSV simulations in Fig. 11

| | $t = 2$ s | | $t = 5$ s | | $t = 8$ s | | $t = 12$ s | |
|---|---|---|---|---|---|---|---|---|
| | **VAM** | **dSV** | **VAM** | **dSV** | **VAM** | **dSV** | **VAM** | **dSV** |
| $L$(m) | 0.762 | 0.925 | 0.817 | 1.054 | 0.921 | 1.138 | 0.852 | 0.884 |
| $L^2$(m) | 0.096 | 0.118 | 0.093 | 0.123 | 0.105 | 0.139 | 0.098 | 0.094 |

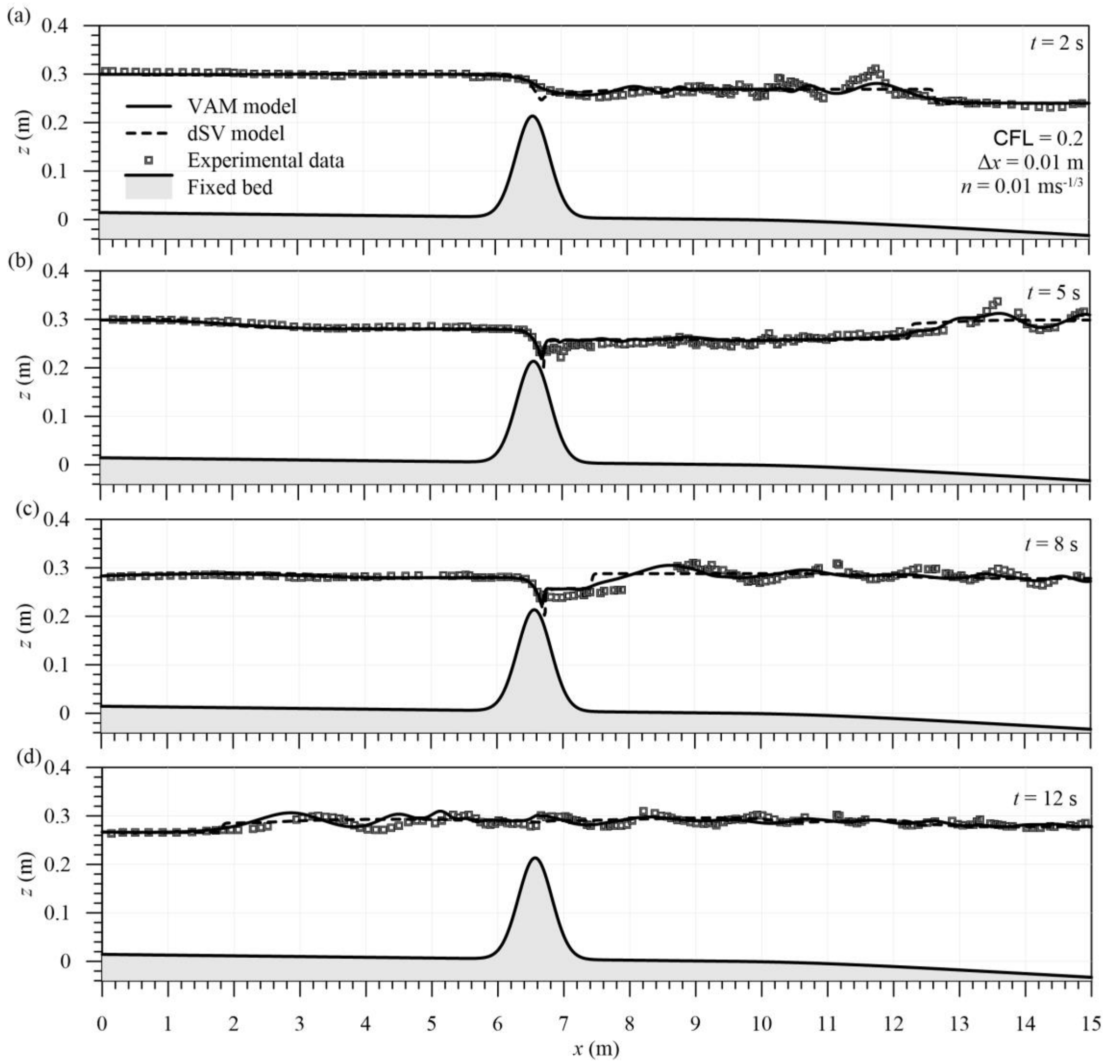


**Fig. 11**. VAM model results for test 3 in comparison with the experimental data and the dSV model predictions at: (a) $t$ = 1 s, (b) $t$ = 5 s, (c) $t$ = 8 s, and (d) $t$ = 12 s.

Figure 12 shows the VAM and dSV model results in comparison with the experimental data extracted for test 4, where $r$ = 0, i.e., dam-break flow under dry bed conditions downstream (Castro-Orgaz and Chanson, 2017). In test 4, the parabolic-like profile of the dry-bed dam-break bore advanced towards the right end of the flume encountering minor bed irregularities at the structural joints, which yielded little free surface perturbations. Right after the reflection of the dam-break bore, two unsteady hydraulic jumps are formed: (i) a moving-forward one at the toe of the lee slope of the obstacle and (ii) a moving-backward one at the front of the reflected bore. Figure 13a shows the experimental data at $t$ = 1 s for the dry-bed dam-break waves at the initial stages, where the VAM model results merely differ from the dSV predictions in the profile of the rarefaction wave. The experimental data at $t$ = 5 s depicts the first instants after the bore reflection, where an unsteady hydraulic jump with smooth transition is developed (Fig. 13b). Here, the VAM model proposed in this study is shown to be unable to tackle the smooth hydraulic jump front, however showing a direct transition, which is in line with the predictions of the dSV model due to the shock detection in this zone. The latter suggests that the turbulence closure may need to be enhanced Some discrepancies have also been found in the prediction of direct hydraulic jumps, as shown in Fig. 12c, $x$ = 11.3 m, for the experimental data at $t$ = 8 s. The last experimental data extracted for test 4 corresponds to $t$ = 12 s (Fig. 12d), where the flow interaction between the two unsteady hydraulic jumps is shown, leading to a challenging turbulence-dominated phenomena. However, the VAM model provides a fair approximation of the test of data showing non-hydrostatic free surface waves after the hydraulic jump. $L$ and $L^2$ norms for VAM and dSV simulations are given in Table 5.

**Table 5.** $L$ and $L^2$ norms for VAM and dSV simulations in Fig. 12

| | $t$ = 1 s | | $t$ = 5 s | | $t$ = 8 s | | $t$ = 12 s | |
|---|---|---|---|---|---|---|---|---|
| | **VAM** | **dSV** | **VAM** | **dSV** | **VAM** | **dSV** | **VAM** | **dSV** |
| $L$(m) | 0.545 | 0.729 | 1.919 | 1.600 | 2.193 | 1.395 | 1.870 | 1.471 |
| $L^2$(m) | 0.076 | 0.097 | 0.342 | 0.281 | 0.303 | 0.163 | 0.246 | 0.204 |

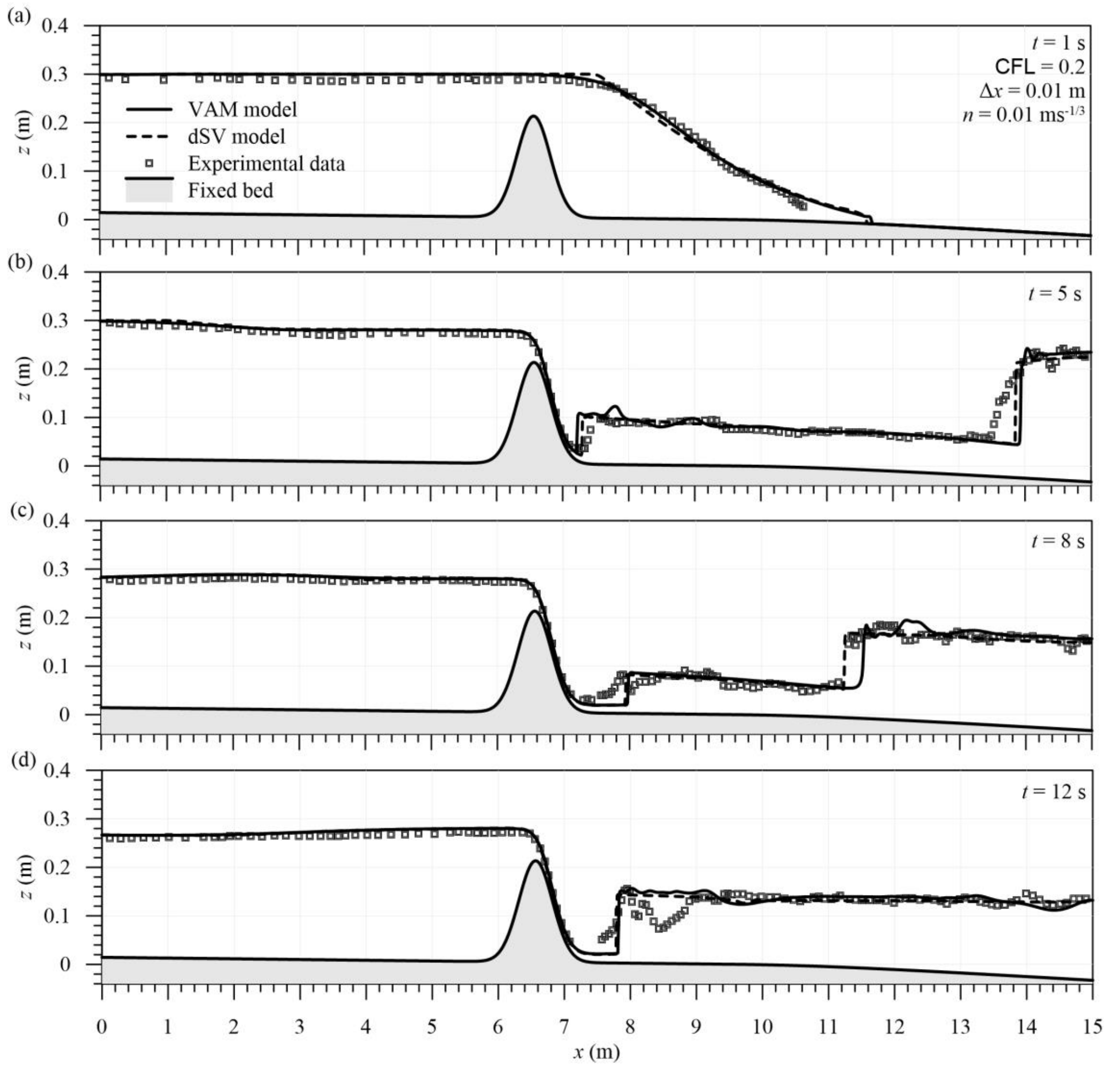


**Fig. 12**. VAM model results for test 4 in comparison with the experimental data and the dSV model predictions at: (a) $t$ = 1 s, (b) $t$ = 5 s, (c) $t$ = 8 s, and (d) $t$ = 12 s.

### *4.3 Steady flow over the obstacle*

A steady flow experiment conducted in this work for the maximum discharge $q$ = 0.1826 $m^2$/s was used (Figs. 13a and b) to validate the VAM model results over an obstacle. The obstacle is a Gaussian profile $z_{bG} = 0.209\cdot\exp[-1/2\cdot((x - x_{crest})/0.254)^2]$, where $z_{bG}$ is the local obstacle height above the flume bed and $x_{crest}$ is the longitudinal location of the crest, installed at $x_{crest}$ = 6.565 m. The experimental obstacle is similar to that of Sivakumaran et al. (1983), but $q$ is higher in the present experiments, and, thus, the degree of non-hydrostaticity of the flow is stronger. In Figure 13, we have included the experimental measurements of the free surface profile $z_s(x)$ and piezometric bed pressure head $(p_b/\gamma+z_b)(x)$ in this obstacle model. Comparison of the simulated results for the free surface and bed piezometric pressure head $p_b/\gamma+z_b$ obtained from the VAM model in Fig. 13 shows the accuracy of this shallow-water formulation predicting the flow features over the obstacle. The mesh-size independence of the results was evaluated progressively reducing $\Delta x$ and CFL.

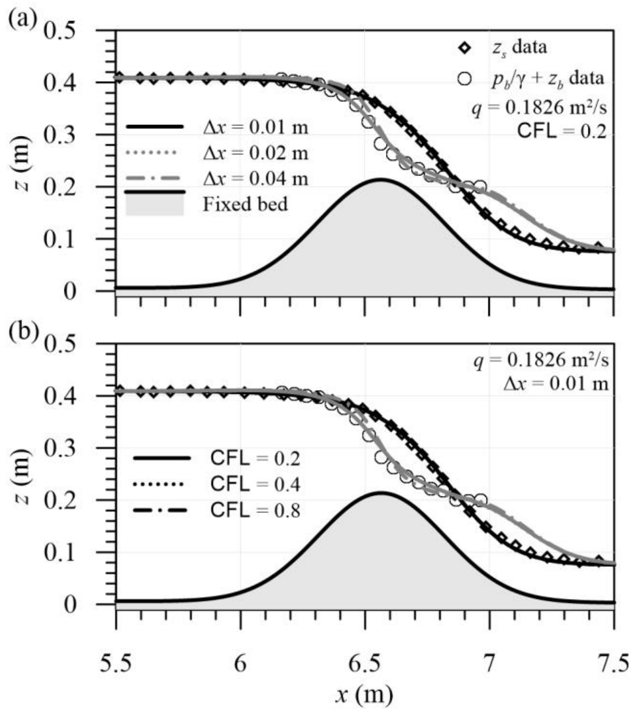


**Fig. 13**. Comparison of steady flow experiments over the obstacle with numerical simulations for the free surface and piezometric bed pressure head

## 5. Conclusions

A new experimental procedure to investigate wave interaction and flow adjustment over obstacles is presented by constructing a large-scale obstacle model in a flume equipped with a wave-generation mechanism based on a dam-break like set-up. The experiments were used to produce a variety of relevant phenomena over topography, as broken and dispersive undular waves, hydraulic jumps, non-hydrostatic critical flow over a sill crest and wave reflection. In addition to the novelty of the procedure to study flow interaction with obstacles, the experimental database generated is itself of utility for environmental fluid flow modelers, given that it can be directly used as benchmark test cases while testing their models. Steady flow tests were used additionally to determine the dynamic fluid pressures over the obstacle.

A new shallow-water weighted-averaged residual model with the ability to mimic turbulent breaking processes trough the formation of shocks or moving hydraulic jumps is presented. This is due to the inclusion of the turbulent velocity profile and Reynolds stresses into the model equations, with a new shock-detection algorithm conferring robustness to the numerical solver. Dispersive effects and non-hydrostatic bed pressures are further tackled by the model given the inclusion of the vertical accelerations. These features make the weighted-averaged residual model presented a suitable tool for environmental modeling of flows over topography with sills.

The turbulent flow model developed reproduces the main features observed during experimentation, namely undular and broken surges, dispersive wave reflection, hydraulic jumps and non-hydrostatic critical flow at sill crest with high non-hydrostatic pressures, with enough accuracy for practical modeling purposes. The dispersionless dSV equations, which is the frequent shallow water flow representation used to study flow adjustment over obstacles, produces only rough estimates or simply does not reproduce the observed experimental phenomena.

The main outcome of this research is a contribution to the physical understanding of the flow adjustment over an obstacle with the new experiments conducted, and by producing a new and robust shallow-water solver with capabilities to deal with several hydraulic phenomena not accounted for in other solvers.

## Acknowledgements

The work of O. Castro-Orgaz, project leader, was supported by the Spanish projects CTM2017-85171-C2-1-R and PID2020-114688RB-I00, and grant María de Maeztu for Centers and Units of Excellence in R&D (Ref. CEX2019-000968-M). FNCC was partly funded by MCIN/AEI/10.13039/501100011033 and the NextGeneration EU/PRTR through Juan de la Cierva program (IJC2020-042646-I) and a "Selection of Doctoral Researchers" grant by the Junta-de-Andalucía government, Spain (Ref. DOC_00996). RJB was partly funded by MCIN/AEI /10.13039/501100011033 through Juan de la Cierva program (IJC2019-038848-I). We thank the two anonymous reviewers of this work for the comments offered to improve it.

## Data availability

The experimental database generated is available as supplementary material in the file "Experiments_EMS2022.xls".

## References

Aureli, F., Maranzoni, A., Mignosa, P., & Ziveri, C. (2008). A weighted surface-depth gradient method for the numerical integration of the 2D shallow water equations with topography. Advances in Water Resources, 31(7), 962−974. https://doi.org/10.1016/j.advwatres.2008.03.005

Bayon, A., Valero, D., García-Bartual, R., & López-Jiménez, P. A. (2016). Performance assessment of OpenFOAM and FLOW-3D in the numerical modeling of a low Reynolds number hydraulic jump. Environmental Modelling & Software, 80, 322−335. https://doi.org/10.1016/j.envsoft.2016.02.018

Bermudez, A., & Vazquez, M. E. (1994). Upwind methods for hyperbolic conservation laws with source terms. Computers & Fluids, 23(8), 1049−1071. https://doi.org/10.1016/0045-7930(94)90004-3

Cantero-Chinchilla, F. N., Bergillos, R. J., & Castro-Orgaz, O. (2020). Nearshore coastal flow processes using weighted-averaged equations. Ocean Engineering, 211, 107480. https://doi.org/10.1016/j.oceaneng.2020.107480

Cantero-Chinchilla, F. N., Castro-Orgaz, O., & Khan, A. A. (2018). Depth-integrated nonhydrostatic free-surface flow modeling using weighted-averaged equations. International Journal for Numerical Methods in Fluids, 87(1), 27−50. https://doi.org/10.1002/fld.4481

Castro-Orgaz, O., & Chanson, H. (2017). Ritter's dry-bed dam-break flows: Positive and negative wave dynamics. Environmental Fluid Mechanics, 17(4), 665−694. https://doi.org/10.1007/s10652-017-9512-5

Castro-Orgaz, O., & Hager, W. H. (2013). Velocity profile approximations for two-dimensional potential open channel flow. Journal of Hydraulic Research, 51(6), 645–655. https://doi.org/10.1080/00221686.2013.809387

Castro-Orgaz, O., & Hager, W. H. (2019). Shallow water hydraulics. Springer, Switzerland. http://refhub.elsevier.com/S0022-1694(21)00309-7/h0030

Castro-Orgaz, O., & Hager, W.H. (2017). Non-hydrostatic free surface flows. Advances in Geophysical and Environmental Mechanics and Mathematics. Springer, Berlin. https://link.springer.com/book/10.1007/978-3-319-47971-2

Cea, L., Bermúdez, M., & Puertas, J. (2011). Uncertainty and sensitivity analysis of a depth-averaged water quality model for evaluation of Escherichia Coli concentration in shallow estuaries. Environmental Modelling & Software, 26(12), 1526−1539. https://doi.org/10.1016/j.envsoft.2011.08.001

Denton, R. A. (1987). Locating and identifying hydraulic controls for layered flow through an obstruction. Journal of Hydraulic Research, 25(3), 281−299. https://doi.org/10.1080/00221688709499271

Farmer, D. M., & Denton, R. A. (1985). Hydraulic control of flow over the sill in Observatory inlet. Journal of Geophysical Research: Oceans, 90(C5), 9015−9068. https://doi.org/10.1029/JC090iC05p09051

Finlayson, B.A., & Scriven, L.E. (1966). The method of weighted residuals- A review. Applied Mechanics Reviews, 19(9), 735−748.

Fischer, H. B., List, E. J., Koh, R. C. Y., Imberger, J., & Brooks, N. H., (1979). Mixing in Inland and Coastal Waters. Academic Press, London. http://refhub.elsevier.com/S1750-5836(21)00139-0/sbref0026

Gamero, P., Bergillos, R. J., Cantero-Chinchilla, F. N., & Castro-Orgaz, O. (2020). A MATLAB software platform for modelling vertically-integrated non-hydrostatic flows with moment equations. Environmental Modelling & Software, 127, 104674. https://doi.org/10.1016/j.envsoft.2020.104674

Ghamry, H. K., & Steffler, P. M. (2002a). Effect of applying different distribution shapes for velocities and pressure on simulation of curved open channels. Journal of Hydraulic Engineering, 128(11), 969−982. https://doi.org/10.1061/(ASCE)0733-9429(2002)128:11(969)

Ghamry, H. K., & Steffler, P. M. (2002b). Two dimensional vertically averaged and moment equations for rapidly varied flows. Journal of Hydraulic Research, 40(5), 579−587. https://doi.org/10.1080/00221680209499902

Gualtieri, C., & Chanson, H. (2021). Physical and numerical modelling of air-water flows: An Introductory Overview. Environmental Modelling & Software, 143, 105109. https://doi.org/10.1016/j.envsoft.2021.105109

Houghton, D.D., & Kasahara, A. (1968). Nonlinear shallow fluid flow over an isolated ridge. Communications on Pure and Applied Mathematics, 21, 1−23. http://dx.doi.org/10.5065/D6G15XS0

Katopodes, N.D. (2019). Free surface flow: Computational methods. Butterworth-Heinemann, Oxford, UK.

Khan, A. A., & Steffler, P. M. (1996a). Vertically averaged and moment equations model for flow over curved beds. Journal of Hydraulic Engineering, 122(1), 3−9. https://doi.org/10.1061/(ASCE)0733-9429(1996)122:1(3)

Khan, A. A., & Steffler, P. M. (1996b). Modeling overfalls using vertically averaged and moment equations. Journal of Hydraulic Engineering, 122(7), 397−402. https://doi.org/10.1061/(ASCE)0733-9429(1996)122:7(397)

Lai, W., & Khan, A. A. (2018). Numerical solution of the Saint-Venant equations by an efficient hybrid finite-volume/finite-difference method. Journal of Hydrodynamics, 30(2), 189−202. https://doi.org/10.1007/s42241-018-0020-y

Liang, Q., & Marche, F. (2009). Numerical resolution of well-balanced shallow water equations with complex source terms. Advances in Water Resources, 32(6), 873−884. https://doi.org/10.1016/j.advwatres.2009.02.010

Long, R.R. (1954). Some aspects of the flow of stratified fluids II, experiments with a two-fluid system. Tellus, 5, 42−58. https://doi.org/10.1111/j.2153-3490.1954.tb01100.x

Long, R.R. (1970). Blocking effects in flow over obstacles. Tellus, 22, 471−480. https://doi.org/10.3402/tellusa.v22i5.10241

Nadiga, B. T., Margolin, L. G., & Smolarkiewicz, P. K. (1996). Different approximations of shallow fluid flow over an obstacle. Physics of Fluids, 8(8), 2066−2077. https://doi.org/10.1063/1.869009

Naghdi, P.M., & Vongsarnpigoon, L. (1986). The downstream flow beyond an obstacle. Journal of Fluid Mechanics, 162, 223−236. https://doi.org/10.1017/S0022112086002021

Pratt, L.J. (1983). A note on nonlinear flow over obstacles. Geophys. Astrophys. Fluid Dynamics, 24, 63−68. https://doi.org/10.1080/03091928308209058

Pratt, L.J., Whitehead, J.A. (2007). Rotating Hydraulics. Nonlinear Topographic Effects in the Ocean and Atmosphere. Springer, Berlin.

Rodi, W. (1993). Turbulence Models and Their Application in Hydraulics. IAHR monograph, Taylor and Francis, London.

Sivakumaran, N. S., Tingsanchali, T., & Hosking, R. J. (1983). Steady shallow flow over curved beds. Journal of Fluid Mechanics, 128, 469−487. https://doi.org/10.1017/S0022112083000567

Steffler, P. M., & Jin, Y. C. (1993). Depth averaged and moment equations for moderately shallow free surface flow. Journal of Hydraulic Research, 31(1), 5−17. https://doi.org/10.1080/00221689309498856

Thacker, W. C. (1981). Some exact solutions to the nonlinear shallow-water wave equations. Journal of Fluid Mechanics, 107, 499−508. https://doi.org/10.1017/S0022112081001882

Toro, E. F. (2001). Shock-capturing methods for free-surface shallow flows. Singapore: John Wiley & Sons. http://refhub.elsevier.com/S0021-9991(20)30628-8/bib00F782AA4A2F153D5CF45E460B244359s1

Toro, E. F. (2009). Riemann solvers and numerical methods for fluid dynamics: a practical introduction. Berlin: Springer. https://link.springer.com/book/10.1007/b79761

Zhou, J. G., Causon, D. M., Ingram, D. M., & Mingham, C. G. (2002). Numerical solutions of the shallow water equations with discontinuous bed topography.

International Journal for Numerical Methods in Fluids, 38(8), 769−788. https://doi.org/10.1002/fld.243

Zhu, D.Z., & Lawrence, G.A. (1998). Non-hydrostatic effects in layered shallow water flows. Journal of Fluid Mechanics, 355, 1−16. https://doi.org/10.1017/S0022112097007611